UNIVERSITY OF CALIFORNIA

SANTA CRUZ

GREENLAND ICE SHEET RETREAT SINCE THE LITTLE ICE AGE

A thesis submitted in partial satisfaction
of the requirements for the degree of

MASTER OF SCIENCE

in

EARTH SCIENCES

by

Marci J. Beitch

June 2014

The Thesis of Marci J. Beitch
is approved:

_____
Professor Slawek Tulaczyk, Chair

_____
Professor Eli A. Silver

_____
Professor Noah J. Finnegan

_____
Tyrus Miller
Vice Provost and Dean of Graduate Studies

Table of Contents

List of Figures

List of Tables

ABSTRACT

Marci J. Beitch

Greenland Ice Sheet Retreat Since the Little Ice Age

Late 20th century and 21st century satellite imagery of the perimeter of the Greenland Ice Sheet (GrIS) provide high resolution observations of the ice sheet margins. Examining changes in ice margin positions over time yield measurements of GrIS area change and rates of margin retreat. However, longer records of ice sheet margin change are needed to establish more accurate predictions of the ice sheet's future response to global conditions. In this study, the trimzone, the area of deglaciated terrain along the ice sheet edge that lacks mature vegetation cover, is used as a marker of the maximum extent of the ice from its most recent major advance during the Little Ice Age. We compile recently acquired Landsat ETM+ scenes covering the perimeter of the GrIS on which we map area loss on land-, lake-, and marine-terminating margins. We measure an area loss of 13,327 ± 830 km², which corresponds to 0.8% shrinkage of the ice sheet. This equates to an averaged horizontal retreat of 363 ± 69 m across the entire GrIS margin. Mapping the areas exposed since the Little Ice Age maximum, circa 1900 C.E., yields a century-scale rate of change. On average the ice sheet lost an area of 120 ± 16 km²/yr, or retreated at a rate of 3.3 ± 0.7 m/yr since the LIA maximum.

Acknowledgments

This project was funded by NASA grant NNX11AH61G. Additional support came from graduate student fellowships and teaching assistantships offered by the UCSC Earth & Planetary Sciences (EPS) department. I appreciate the extra teaching assistantship opportunities amidst US government sequestration of NASA funds.

I would like to thank my Thesis advisor, Dr. Slawek Tulaczyk, for the opportunities of polar research, as well as his guidance and support. I would also like to thank my graduate advisor, Dr. Susan Schwartz, and the EPS administrative staff for helping navigate the graduate experience. I am grateful and honored to have Dr. Eli Silver, Professor of Remote Sensing, and Dr. Noah Finnegan, Professor of GIS and Geomorphology, serve on my Thesis reading committee. I appreciate their guidance and support. I acknowledge the EPS Glaciology group members who were mentors and comrades throughout this project, especially Nicholas Geier for his commitment and stamina in the trimzone mapping efforts. Field opportunities in Alaska and Antarctica with the Glaciology group and the WISSARD, MIDGE, and VALKYRIE projects have been highlights of my graduate career.

I acknowledge Dr. Bea Csatho at the University of Buffalo, New York for providing GPS data and scientific materials of the trimzone studies she led, as well as her guidance and collaboration throughout this project. I also acknowledge Dr. Paul Morin and Claire Porter at the University of Minnesota Polar Geospatial Center for providing WorldView imagery.

Dedication

To my wonderful family and friends who inspire purpose, meaning, and greatness.

1 INTRODUCTION

Remote sensing studies from the recent satellite era document high resolution ice sheet responses to climate forcing but are limited in their temporal coverage to the last several decades. Where historical data are available, studies of ice margin changes can extend further back in time but tend to be limited in their spatial coverage. The study presented here builds on previous work by *Csatho et al.* [2005] of the Jakobshavn Isbræ region in western Greenland in which Little Ice Age (LIA) trimzones (vegetation poor land areas exposed by recent glacier retreat) are used to quantify ice margin retreat since the LIA glacial maximum (circa late 1800s to early 1900s C.E.). We expand trimzone mapping to the entire Greenland Ice Sheet (GrIS) perimeter using recent Landsat Enhanced Thematic Mapper Plus (ETM+) imagery. This yields a high resolution, wide scale dataset of ice sheet area loss since the LIA and places recently measured ice margin changes in a century-scale context.

Recent temperature increases have been expressed more severely at high latitudes, especially in the Arctic [*Jones and Moberg*, 2003]. This region hosts the GrIS, which is situated between ~ 60 and 83 ˚N latitude (Figure 1). The island of Greenland is surrounded by the Arctic Ocean to the north, the Atlantic Ocean to the east and south, and Baffin Bay to the west. The ice sheet covers a surface area of ~ 1.805×10^6 km² (including separated ice caps and local glaciers) [*Kargel et al.*, 2012] and hosts an estimated ice volume of 2.96×10^6 km³ (a sea level equivalent of 7.36 m) [*Bamber et al.*, 2013]. Because of its location in relatively low latitudes of the northern hemisphere, as compared to the high southern latitudes of the Antarctic Ice Sheet,

near future shrinkage of the GrIS poses potentially large threats to coastal natural systems and human infrastructure [*NRC*, 2012; *IPCC*, 2013].

Satellite observations of the Earth have allowed scientists to view changes over large portions of the planet since the 1980s and early 1990s (e.g., Landsat, ERS). Scientific focus shifted to the polar regions in the late 1990s and implementations of new sensors (e.g., ASTER, GRACE, ICESat, MODIS, RADARSAT, SPOT) monitor recent changes in snow and ice conditions in increasing detail. Many scientific studies report thinning and retreat of polar ice sheets, especially the GrIS, at accelerating rates over the past three decades [*Moon and Joughin*, 2008; *Howat and Eddy*, 2011; *Zwally et al.*, 2011; and others]. Additionally, advancing numerical ice sheet and climate models provide improving predictions of the near future global effects of shrinking ice (e.g., sea level rise, increased albedo) [*Price et al.*, 2011; *Rae et al.*, 2012; *Hanna et al.*, 2013]. Additional studies are needed to document the state of the cryosphere and to improve modeling of its near future evolution.

2 LITERATURE REVIEW

2.1 Remote Sensing Mapping of Ice Margin Retreat

Several studies synthesize available aerial- and satellite-derived data to document the response of the GrIS to northern hemisphere temperature increases seen in the recent decades. *Howat and Eddy* [2011] report on the be-

havior of 210 marine terminating glaciers on Greenland's coast between the years 1972 and 2010 where covered by Landsat imagery. In the earlier time periods (pre-1992) subsets of the glaciers display some retreat and some advance of the glacier fronts on the order of tens of m/yr. In the later time periods (post-1992) nearly all glaciers retreat on the order of tens to hundreds of m/yr with a few greater than 1 km/yr [*Howat and Eddy*, 2011]. *Moon and Joughin* [2008] report similar results from 206 glaciers terminating in the ocean, ice shelf, or on land from the years 1992-2007. The land-terminating glaciers show little change, while the marine terminating glaciers show increasing rates of retreat from the time periods 1992-2000 and 2000-2006. Glaciers in the SE generally advance in 2006-2007, likely responding to locally cooler temperatures during that year [*Moon and Joughin*, 2008], but have since been experiencing an increase in their ice velocities as shown from synthetic aperture radar data [*Moon et al.*, 2012].

Datasets dating to the 1980s or earlier are available for smaller portions of the GrIS and select glaciers [*Csatho et al.*, 2008; *Bjørk et al.*, 2012; *Kjær et al.*, 2012]. Aerial photographs and historical records provide longer term perspectives on regional ice margin changes. *Kjær et al.* [2012] show elevation changes of marginal ice in NW Greenland for 1985-2005 and 2005-2010 and reveal a dramatic increase in the rate of thinning in the latter time period. *Bjørk et al.* [2012] utilize historic aerial photography dating back to the 1930s to build a record of retreat, advance, and further retreat of Green-

land's SE ice margin at nearly decadal temporal resolution. In the 1930s regional warming triggered a retreat, although the current (2000-2010) scale of retreat is far greater [*Bjørk et al.*, 2012]. *Csatho et al.* [2008] use historical records and aerial photography, paired with recently acquired satellite data to build a detailed history of thinning and retreat of the Jakobshavn Isbræ glacier in western Greenland throughout the 20th and 21st centuries. Thinning and retreat occurred here in pulses of relatively rapid change amidst periods of slower change, likely in response to regional warming [*Csatho et al.*, 2008]. A cooling trend caused the glacier to thicken and advance from 1985-1997 but since the late 1990s, warming in the region has triggered rapid thinning and retreat that began in the late 1990s and continues through today [*Csatho et al.*, 2008; *Holland et al.*, 2008; *Briner et al.*, 2011; *Neilsen et al.*, 2013].

2.2 Marginal Trimzone Mapping and the Age of its Outer Limit

In order to reach further back in time, past glacier margin positions can be inferred from indicators in the recently deglaciated landscape. Moraine mapping, cosmogenic and radiocarbon dating, as well as analyses of sediment cores from lakes, constrain century- to millennial-scale ice margin positions. A Holocene record of ice retreat in Greenland has been inferred from a combination of these techniques. General retreat dominates the Holocene and occurs in pulses that are also punctuated by periods of cooling and readvance [*Ten Brink and Weidick*, 1974; *Csatho et al.*, 2008; *Briner et al.*, 2010, 2011;

Young et al., 2011; *Kelley et al.*, 2012]. The most recent advance occurred during the LIA from about the 14th to 19th centuries [*Grove*, 2001]. The LIA was a period of general cooling in the northern hemisphere in which temperatures were about 1 ˚C colder than today [*Dahl Jensen et al.*, 1998; *Lemke et al.*, 2007]. Climate proxies and temperature records indicate that temperatures began to increase around 1850 C.E., ending the LIA [*Dahl Jensen et al.*, 1998; *Mann et al.*, 2009; *Ljungqvist et al.*, 2012] but, as expected, the GrIS exhibited a lagged response of its glacier extent to post-LIA warming [*Weidick*, 1968; *Box et al.*, 2009; *Box and Colgan*, 2013].

The LIA maximum extent of the GrIS is observed as the sharp vegetation boundary roughly parallel to the present ice margin that is called the trimline. The trimline separates mature lichen-dominated growth on bedrock and older glacial deposits from the recently exposed proglacial land whose vegetation was scraped away by the movement of the overriding glacier [*Flint*, 1971; *Beschel and Weidick*, 1973; *Csatho et al.*, 2005, 2008]. In western Greenland the crust lichen *Rhizocarpon* spp. is the dominant species whose growth in its first seven decades is especially slow; maximum growth has been measured on moraines dated to around 1000 years in age [*Beschel and Weidick*, 1973]. Due to lichen's slow establishment and growth rate on newly exposed rock surfaces, the land areas exposed in the century since the LIA maximum, called trimzones, exhibit very little lichen regrowth. Thus the trimzones maintain a

visible and obvious difference from lichen-covered land that was not glaciated during the LIA glacial advance.

Historical records suggest that the LIA maximum occurred between 1880 and 1890 C.E. in western Greenland [*Beschel and Weidick*, 1973]. *Ten Brink and Weidick* [1974] examine Holocene glacier fluctuations in West Greenland, East Greenland, and the eastern Canadian Arctic and find similarity in glacier response, indicative of climatic change affecting the entire region. They postulate that the LIA maximum for the whole island of Greenland can be constrained to the years 1880-1920 C.E. Their conclusion is largely based on historical records, moraine mapping, and lichen dating in West Greenland, but is accepted to represent the timing across the GrIS as a whole [*Ten Brink and Weidick*, 1974]. Further, *Björnsson et al.* [2013] report similarity in the onset of the post-LIA recession of Icelandic glaciers, which began in the 1890s C.E.

To measure the GrIS response to the transition from the LIA, *Box and Colgan* [2013] use meteorological station and ice core data combined with regional climate model output to produce a reconstruction of GrIS total mass balance for the time period 1840 to 2010 C.E. Their results indicate that the GrIS maintains near zero mass balance through the end of the 19th century. Around the year 1900 C.E., the ice sheet mass balance becomes negative, a state that dominates the remainder of the century and continues to 2010, the end of the observation period. The switch to mass deficit in 1900 C.E. is due

to an increase in runoff and a decrease in accumulation. In the year 1900 C.E. the GrIS begins contributing to sea level rise following the near zero trend in sea level contribution from 1840 to 1900 C.E. Henceforth, we assume that the sharp transition from negative to positive sea level contribution around 1900 C.E. represents the most likely timing for the LIA maximum extent of the GrIS margins, which then switch to retreat mode [*Box and Colgan*, 2013].

A decadal time scale of the response of GrIS surface mass balance and runoff is observed in the *Box and Colgan* [2013] study. They find 11 and 13 years to be the peak sensitive time scales for surface mass balance and runoff, respectively [*Box and Colgan*, 2013]. The *Box and Colgan* [2013] study, historical records, moraine mapping, and lichen dating help to constrain the timing of the LIA maximum to around the year 1900 C.E. with an uncertainty of 10 to 20 years. For the purposes of our study the LIA maximum glacial extent, as represented by the outer limit of the marginal trimzone in Greenland, is considered to have occurred in the year 1900 ± 13 years C.E.

3 STUDY AREA

Our study examines the area loss of the main body of the GrIS, which is also referred to as the inland ice, since the LIA glacial maximum (Figure 1). The inland ice area loss along the land-terminating margins of the ice sheet is expressed as trimzones, whose area is bounded on the inside by the current ice sheet margin and on the

outside by the vegetation trimline that roughly parallels the ice sheet edge [*Weidick*, 1968; *Csatho et al.*, 2005, 2008; *Kelley el at.*, 2012]. Trimzones are also present along marine fjord walls and on land surrounding lakes that are adjacent to the inland ice, which indicate area loss along marine- and lake-terminating ice margins. The water-covered ice margins are also examined in our study of inland ice area loss (Figure 2).

Greenland also hosts smaller ice caps and isolated glaciers not connected to the inland ice that contain LIA trimzone areas [*Weidick*, 1968; *Citterio et al.*, 2009] but are not included in this study.

4 METHODS

4.1 Satellite Imagery

We observe the GrIS margins on satellite imagery collected from three sensors: Landsat, ASTER, and WorldView, as described below.

4.1.1 Landsat ETM+

This study uses Landsat ETM+ (also referred to as Landsat 7) scenes downloaded from the USGS Global Visualization Viewer (GloVis) website (glovis.usgs.gov; Figure 1). The cross track coverage of the Landsat ETM+ sensor is 183 km, providing scene footprints of approximately 180 km × 180 km [*Markham et al.*, 2004]. Eight spec-

tral bands are composed of three bands in the visible spectrum (0.452-0.514, 0.519-0.601, and 0.631-0.692 μm), one band in the near-infrared (0.772-0.898 μm), and two bands in the middle-infrared (1.547-2.346 μm) with spatial resolutions of 30 m; one thermal band (10.31-12.36 μm) with a spatial resolution of 60 m; and one panchromatic band (0.515-0.896 μm) with a spatial resolution of 15 m [*Chandler et al.*, 2009].

Boreal summer images of the ice sheet perimeter and adjacent land are selected based on their lack of cloud and snow coverage. Images from the boreal summers of 2012, 2011, and 2010 make up 91% of the 224 images used to build the ice sheet perimeter coverage, with 2012 images being the majority. Few images gathered in boreal summers of 2009 and 2007 supplement the coverage where 2010-2012 mostly clear images are not available (Table 2). The mean year of the Landsat images used is 2011 with a standard deviation of 1 year.

An additional scene of southern Greenland collected in August 1992 from the Landsat 5 Thematic Mapper (TM) sensor is used in a case study of area loss rate comparisons from the LIA to 1992 and from 1992 to the present. The case study is explained further in Sections 4.1.3 and 5.2.3.

4.1.1.1 Mosaicking

Images used in this study were collected after the 2003 Landsat 7 scan line corrector failure [*Markham et al.*, 2004]. The images used contain stripes of no data, which are mostly eliminated when multiple images of the same location (separated by as little time as possible), are mosaicked one on top of the other. The mosaicking program in the ENVI remote sensing software ignores values of no data so stripes are filled in with data from the underlying image(s). This method is also used in *Howat and Eddy* [2011].

4.1.1.2 Multispectral Displays

Band combinations using Landsat ETM+ visible and near-infrared bands are used to highlight spectral differences between ice, snow, water, land, and vegetation. Chiefly, the Landsat bands 4 (near-infrared), 3 (visible, red), and 2 (visible, green) displayed in the Red-Green-Blue combination, respectively, show great contrast between ice and land. In this combination, which is also called the visible near-infrared (VNIR) display, vegetation, having a high reflectance in the near-infrared, appears red [*Knipling*, 1970]. Extensive vegetative cover on red-colored land is distinct from land without signifi-

cant vegetation, which appears gray or brown, sometimes with a faint red tint (Figure 2).

Field studies have documented that lichen-dominated vegetation is widespread on ice-free land in Greenland and that coverage of mature lichen specimens serves as an indicator of unglaciated land during the LIA [*Beschel and Weidick*, 1973; *Csatho et al.*, 2005]. Since new lichen growth is slow to establish, specimens are small and scattered, thus do not express a strong spectral signature on the recently exposed land [*Beschel and Weidick*, 1973]. The sharp transition from relatively high-biomass vegetation to very little vegetation on land parallel to the current ice sheet edge is the outer trimzone boundary (the trimline) that we map on the Landsat band 4-3-2 combination (Figure 2).

4.1.2 WorldView

Very high spatial resolution WorldView imagery supplied by University of Minnesota's Polar Geospatial Center supplements our study. A mosaic of images of the Jakobshavn Isbræ region collected in the boreal summer months of the years 2009-2011 is used as a reference to test the accuracy of our Landsat-mapped ice edge, discussed in Section 5.1 (Figure 3). The WorldView mosaic is composed of pan-

chromatic images that have spatial resolution of 0.5 m [*Alkan et al.*, 2013].

4.1.3 ASTER

As part of the more in depth look at the longer- and shorter-term area loss and retreat rates in South Greenland mentioned in Section 4.1.1, a scene from the Advanced Spaceborne Thermal Emission and Reflection Radiometer (ASTER) sensor collected in August 2000 and downloaded from the GloVis website, supplements our study. The ASTER scene has a footprint of approximately 60 km × 60 km. We utilize the three VNIR bands of the sensor (bands 1, 2, and 3N), collecting spectral information from wavelengths 0.556-0.807 μm with spatial resolutions of 15 m [*Sakuma et al.*, 2005]. The ASTER scene from 2000 accompanies the 1992 and 2012 Landsat scenes of the same area in a case study of the local changing area loss and retreat rates (Figure 4).

4.2 Mapping Inland Ice Area Loss

The data collection of the inland ice area loss is performed in two stages: first, mapping the land area exposed since the LIA maximum expressed as trimzones, and second, mapping the marine and lake zones of ice sheet area loss as interpreted from the trimzone mapping.

4.2.1 Mapping Area Loss on Land

Trimzones, which represent the ice area loss on land, are mapped on the Landsat image mosaics displayed in the 4-3-2 band combination in ENVI. Using the vector polygon tool one observer visually determines and manually digitizes the trimzones, producing many enclosed polygons along the ice sheet margin. Trimzones are often mapped as long, thin polygons that follow the trend of the current ice edge (Figure 2). The areas enclosed by the polygons, when summed together, give the horizontal land surface area exposed by retreating glaciers since the LIA maximum. Trimzones are thinner in areas of little ice sheet retreat and/or steep topography and wider in areas of large ice sheet retreat and/or low relief. Some steep north-facing slopes exhibit shadows along the ice margins they border. We are not able to observe trimzones in the shadowed regions so they are not mapped if they are present but we estimate that unobserved trimzones in shadows account for less than 1% of the total ice sheet area loss, which is insignificant relative to the scale of our study. Trimzones on nunataks within the inland ice are mapped as part of this study.

Some glacial outwash plains, very steep slopes, and land with nearly year-round snow cover resemble trimzone areas in the VNIR color display but are determined not to be trimzones since they lack

the position and similar manifestation of trimzones in the local setting. Conversely, some trimzones include patches of red in the VNIR display that are determined to be red due to the presence of annual grassy or tundra vegetation that established on the recently unglaciated land faster than lichen communities. The red patches from the grassy and tundra vegetation do not exhibit patterns related to the LIA maximum extent of the ice sheet, therefore are included in a trimzone if a sharper trimline is observed outside their extents. We review scientific literature of more in depth studies along smaller portions of the ice sheet, maps of ice sheet extent, and higher resolution imagery on Google Earth where available to compare and augment our trimzone mapping [*Weidick*, 1968, 1995; *Weidick et al.*, 2004; *Csatho et al.*, 2005, 2008; *Howat and Eddy*, 2011; *Johannessen et al.*, 2011; *Bjørk et al.*, 2012; *Kargel et al.*, 2012; *Kelley et al.*, 2012; *Kjær et al.*, 2012; *Citterio and Ahlstrøm*, 2013; *Lea et al.*, 2014].

The method of manual digitation allows for careful determination of trimzone areas where they may or may not be exhibited in their usual form. We realize human biases are inherent in manual analyses, thus biases are calculated and included in our measurement errors. The error analysis is discussed in Section 5.1.

4.2.2 Mapping Area Loss of Marine and Lake Zones

The second stage of data collection focuses on the zones of ice sheet area loss along the marine- and lake-terminating margins, which are termed marine and lake zones, respectively. A second observer performs this mapping. Since trimzones are only visible on land, the water-covered areas of ice sheet area loss are interpreted by trimzones mapped on the surrounding land. For example, the marine zone of a glacier that outlets into an ocean-connected fjord is interpreted to encompass the area of the fjord bounded by the current ice margin, the trimzones mapped along the fjord walls, and a straight line drawn across the fjord that connects the furthest extent of each fjord wall trimzone (Figure 5A). The polygon is classified as a marine zone of ice sheet area loss. Where fjords are not present along marine-terminating ice margins, often small islands of land near the current ice margin exhibit inland ice trimzones. These trimzones are distinct from local ice cap trimzones because they appear on the side of the island closest to the current ice margin, their color is consistent with trimzones on nearby coasts proximal to the inland ice, and trimzones like these on many neighboring islands taken together parallel the current ice margin. In contrast, trimzones of local ice caps generally circle the highest relief of a mountain range or mountainous island. We map a marine retreat zone polygon encompassing the marine area bordered

by the current ice margin and straight lines drawn between the inland ice trimzones on nearby islands (Figure 5B).

Lakes present along the inland ice margins often have trimzones mapped on the land on either side of the lakes' ice-marginal boundaries. We map a lake zone polygon to encompass the water-covered area bounded by the current ice margin, the edges of the trimzones on either side of the lake, and a straight line connecting the farthest extents of trimzones on either side of the lake (Figure 6A). Trimzones sometimes surround the entire lake, in which case the whole surface area of the lake is mapped as a lake zone of ice sheet area loss (Figure 6B).

Some proglacial lakes have active filling and draining cycles [*Kelley et al.*, 2012]. A lake that has drained may exhibit shorelines that encompass its own former highstand. These shorelines may mimic trimzones on the VNIR display because they are void of vegetation and exhibit sharp boundaries between the lake's outer shoreline boundary and the surrounding vegetated land. Additionally, the shorelines often merge with trimzones along the surrounding ice margins, thus the shorelines could be misinterpreted as LIA trimzones. One area of significant vegetation-free land along a proglacial lake adjacent to the inland ice margin is Lake Tininnilik in central West Greenland, south of Jakobshavn Isbræ. *Kelley et al*. [2012] conducted studies in

this area and determined that the vegetation-free land surrounding the lake observed on 2010 imagery was due to a former highstand of the lake, thus it was not LIA trimzone. In our study if broader trimzones exist that surround the lake and extend along the lake-free margin, the vegetation-free areas are considered trimzones and the lake is mapped as a lake zone of ice sheet area loss. If the vegetation-free zone exhibits strong horizontality across the entire shoreline we consider this to be a 'bathtub ring' of equal elevation, which contrasts with the tendency of ice surfaces to have sloping termini. Hence, we do not include 'bathtub rings' around lakes, nor the lake area, in the ice sheet area loss.

The lake boundaries, associated shorelines, and trimzones are ambiguous in their nature and we exercise caution when determining if they are zones of ice sheet area loss. As with trimzone mapping, we review published literature, maps, and Google Earth to help determine the LIA maximum extent of the GrIS that is covered in water on the Landsat imagery we use. Furthermore, when performing the mapping of marine and lake zones, we believe our method of connecting trimzone areas with straight lines is a conservative estimate of the marine or lake zone area.

4.3 Inland Ice Area Loss by Latitude Bin

To analyze spatial variability of inland ice area loss we define latitudinal zones along the GrIS perimeter. The ice sheet is first separated into two parts, West and East, then divided into two-degree latitude bins spanning 60 to 82 ˚N, the furthest northern coverage of the Landsat satellite (Figure 1). Eleven latitude bins make up each part (e.g., 60 – 62 ˚N, 62 – 64 ˚N, …, and 80 – 82 ˚N in West Greenland and the same in East Greenland). Area loss in each latitude bin is determined by summing the area of the trimzone, lake, and marine zone polygons that lie in each bin. Area loss measurement values are listed in Table 1 and displayed in Figure 7.

The time period elapsed since the LIA maximum is taken to be the year 1900 C.E. subtracted from 2011 (the mean year of Landsat imagery used in this study). The trimzone area values are divided by 111 ± 13 years to give a yearly area loss rate as if area loss has been constant since the LIA maximum (Table 1; Figure 9).

4.4 Latitude Bin Length from NSIDC Ice Sheet Perimeter

We convert area loss to linear retreat in order to calculate an average width of margin retreat in each latitude bin. This also normalizes the area loss values along the irregular ice sheet margin in each bin. For example, a north-south trending segment of the ice sheet margin that is generally perpendicular to lines of latitude (e.g., West Greenland latitude bin 66 – 68 ˚N) is shorter

than another portion that bends west or east (e.g., West Greenland latitude bin 76 – 78 ˚N), thus accounts for a shorter margin of ice sheet area loss measurements. The normalization allows for latitudinal comparisons of area loss widths.

The ice sheet margin length is determined for each bin from a vector of the GrIS perimeter acquired from the National Snow and Ice Data Center (NSIDC) Atlas of the Cryosphere [*Maurer*, 2007]. The vector of the ice sheet is made up of one large ice sheet polygon and many smaller polygons of ice caps not connected to the main body of the ice sheet. These smaller outlines are removed since we do not examine trimzones associated with disconnected ice caps. Where the main outline includes local glaciers and ice caps not examined in our study, we cut their outlines from the vector and adjust the ice sheet margin to follow the outline of the inland ice margin. Where the distinction between inland ice and local glaciers or ice caps is hard to determine, we examine the area in our study and include its outline in the margin length. The vector of the margin is separated into segments of length for each latitude bin. To determine the average horizontal retreat, we divide the area loss by the margin length in each latitude bin (Table 1; Figure 8).

The horizontal retreat values are divided by the time since the LIA maximum to give a yearly retreat rate as if retreat has been constant since the LIA maximum (Table 1; Figure 9).

5 RESULTS

Our results are presented following a discussion of the error analysis that determines our measurement uncertainly.

5.1 Error Analysis

Inherent in our analysis is the systematic error due to the 30-m spatial resolution of Landsat imagery used to build our dataset. The spatial resolution sets a theoretical lower limit on the width of detectable ice sheet area loss since we are not able to map area loss zones if less that 30 m separates the current ice edge from the outer edge of the area loss zone. Furthermore, the uncertainty in the area loss measurements is dependent upon our accuracy and precision in mapping. Thus, we assess how accurately we map the current ice margin and the outer edge of an area loss zone, how precise our mapping is, and the human bias inherent in manual analyses. When assessing the uncertainty in our horizontal retreat measurements we propagate the area loss uncertainty with an error in the length of the ice margin determined for each latitude bin. As such, when calculating the rates of area loss and retreat we assess uncertainty by propagating the area loss and retreat uncertainties with the errors in the estimated age of the LIA maximum. The following discussion of error determinations describes our error analysis for each category of data measured: area loss, horizontal retreat, and rates of area loss and retreat.

5.1.1 Area Loss

The mapping of ice sheet area loss along land and water-terminating ice sheet margins begins with trimzone mapping on land, which then guides the mapping of the area loss encompassed by lake and marine zones. Thus, we focus our error analysis on the method of trimzone mapping and apply the analysis to the marine and lake zones. The accuracy in mapping the trimzones depends on our accuracy in delineating the outer trimzone margin and the inner ice edge margin. To measure our accuracy we compare trimzones mapped from Landsat imagery to field-collected GPS points of the trimline [*Csatho et al.*, 2005] and very high spatial resolution satellite imagery of the ice edge (Figure 3).

We compare our trimline mapping to GPS points of the outer trimline taken as part of the 2003 field mapping campaign near Jakobshavn Isbræ published in *Csatho et al.* [2005]. This comparison quantifies the mismatch between our mapping of the outer trimzone boundary and the location of this boundary defined by field observers. The distances from our Landsat-mapped trimline and the GPS points are given positive values if the points are located outside our trimline (farther from the current ice margin) and negative values if they are inside (closer to the current ice margin). The mean offset is 54 m indicating

that our mapping of the outer trimzone boundary from Landsat data underestimates trimzone width. The standard error associated with the offset is 8.6 m.

We compare our inner trimzone boundary to points along the ice edge collected on very high spatial resolution (0.5 m) WorldView imagery. The mosaic of WorldView imagery chosen for this analysis includes images taken during the boreal summer months, as is the case for our Landsat imagery, but may be separated by one to three years. Since ice margins can change significantly from year to year we select points along ice margins whose movement is not detected on Landsat scenes during the years of the WorldView imagery mosaic. The distances from our Landsat-mapped ice edge and the WorldView ice edge points are given positive values if the points are located outside our ice edge (farther from the outer trimline boundary) and negative values if they are inside (closer to the outer trimline boundary). Similar to the trimline delineation our mapped ice edge underestimates the inner extent of the trimzone by a mean distance of 15 m with a 3.9-m standard error in the measurements. The 15-m underestimation value is less than the 30-m pixel size of the imagery, however, we consider it valid because mapping can be performed with sub-pixel resolution, especially when a pixel captures surfaces with high spectral contrasts (e.g.,

bright snow or ice and dark land or water) [*Kamp et al.*, 2011]. The observer maps the ice edge through the middle of mixed pixels.

Taken together, these underestimations of trimzone width are referred to as the mapping bias. To correct for the mapping bias in our trimzone delineation we propagate the offsets to all our results by extending the outer margin of the trimzones by 54 m and the inner margins by 15 m. This is accomplished by multiplying each underestimation width by half the perimeter length of the trimzone polygons and adding these areas to the trimzone area measured. We use the area of these wider zones in our analysis. The same correction is performed for the areas of the lake and marine zones. The error values associated with the area loss measurements are calculated from the standard errors of the GPS and ice edge point distances to our Landsat-mapped trimzones (8.6 m and 3.9 m, respectively), each multiplied by half the length of the trimzone polygon perimeters and summed. This error is referred to as the mapping error. We recognize that the field GPS data and WorldView imagery come from a restricted region so we report the uncorrected values for comparison (Table 1).

To assess internal precision in our measurements, or our ability to replicate our results, we apply precision-analysis methods discussed in *Paul et al*. [2013] in which the accuracy of mapping glacier margins is assessed. We apply their method of repeat digitizations to six trim-

zone areas representing diverse settings (e.g., different glacier termination types), locations around the ice sheet, and mapping challenges (e.g., debris-covered ice margins, snow cover, and shadowed regions). The standard deviations (as percent values) of five iterations for each of the six areas are averaged to give the internal precision error. This value, referred to as the measurement precision, is 6.6%.

For continuity, one observer digitizes all trimzone areas. A second observer performs the second stage of marine and lake zone mapping. We compare subsets of trimzone digitations performed by both observers to determine a human bias in our mapping. The areas mapped by the two observers differ by 4.1%. Since this value is smaller than the 6.6% measurement precision we assume that the human bias is incorporated into the measurement precision.

Total uncertainty in the area loss measurements is computed by propagation of errors of the two sources of error (mapping error and measurement precision) in which the square root of the sum of the squares of the errors is calculated: $\sigma_A = \sqrt{\sigma_{mapping}{}^2 + \sigma_{precision}{}^2}$, where σ refers to measurement uncertainty and A represents area loss. The uncertainty in our measurements is around 7% but is a greater percent in areas of small, or thin, area loss zones and a smaller percent in areas of large, or wide, area loss zones. This is reflective of the ratio of zone

perimeter to the area encompassed being larger for thinner zones and smaller for wider zones.

5.1.2 Horizontal Retreat

The uncertainty in the averaged horizontal retreat includes the error in the length of the ice sheet margin by which the area loss is divided to give the retreat width. The length of the GrIS margin is determined from a vector of the outline of the Greenland inland ice acquired from the NSIDC Atlas of the Cryosphere [*Maurer*, 2007]. To compute an uncertainty in its length, a detailed ice margin is digitized in-house for a 200-km (map distance) portion of the ice sheet and compared to the length of the NSIDC GrIS perimeter vector for the same 200-km section. The NSIDC length is 44.3% shorter than our manually digitized ice margin with a standard error in the measurements of 18.1%. As described above for the underestimation of trim-zone mapping, the length measurements for latitude-binned sections of the ice sheet from the NSIDC perimeter are extended by 44.3% to account for their underestimation in ice sheet length. Table 1 includes the uncorrected horizontal retreat values (the uncorrected area loss divided by the uncorrected ice sheet length), as well as the corrected values. The error values are calculated from the standard error of the two ice sheet length measurements ($\sigma_L = L \times 18.1\%$) and propagated with the

uncertainty in area loss to give a total uncertainty in horizontal retreat: $\sigma_R = R\sqrt{\left(\frac{\sigma_A}{A}\right)^2 + \left(\frac{\sigma_L}{L}\right)^2}$, where L refers to the length of the ice sheet margin and R refers to the horizontal retreat. The uncertainty in the width of ice sheet retreat since the LIA maximum taken with the uncertainty in the area loss is around 19%.

5.1.3 Rates of Area Loss and Retreat

The uncertainty in the rates of ice sheet area loss and retreat since the LIA integrates the 13 years uncertainty in the timing of the LIA maximum extent (discussed in Section 2.2) and the 1 year standard deviation of the dates of the Landsat images used for our mapping, which signifies the end of the observation period. By propagation of these two errors, $\sigma_t = \sqrt{13^2 + 1^2}$, where t refers to time, the uncertainty in the years passed since the LIA maximum (t = 111 years) is 13 years. The uncertainty in the rate of area loss per year since the LIA maximum propagated with the uncertainty in the area loss is around 14% determined by $\sigma_{r_A} = r_A\sqrt{\left(\frac{\sigma_A}{A}\right)^2 + \left(\frac{\sigma_t}{t}\right)^2}$, where r_A refers to the rate of area loss. The uncertainty in the rate of retreat per year propagated with the uncertainty in the retreat width is around 23% determined by $\sigma_{r_R} = r_R\sqrt{\left(\frac{\sigma_R}{R}\right)^2 + \left(\frac{\sigma_t}{t}\right)^2}$, where r_R refers to the rate of retreat. Table 1

lists the uncorrected area loss and retreat rate values (uncorrected area loss and horizontal retreat values, respectively, divided by 111 years), as well as the corrected values (corrected area loss and horizontal retreat values, respectively, divided by 111 years).

5.2 Main Results

Our measurements quantify the land, lake, and marine area loss since the LIA maximum. This dataset is unique since it is built from modern day, high resolution satellite imagery with high temporal frequency and complete spatial coverage of Greenland's margins south of 82 ˚N latitude. Hence, we are able to map area loss on clear, closely timed images that span the perimeter of the GrIS. The total area loss measured is 13,327 ± 830 km², roughly the size of Death Valley National Park, California's and the contiguous United States' largest national park. Horizontal retreat averaged across the ice sheet perimeter is 363 ± 69 m. The horizontal retreat is a distance that the entire ice sheet may have "stepped-back" if retreat was spatially homogeneous. Retreat was not likely to have been homogeneous, so the value given here is just a spatial average of GrIS retreat. The averaged rates of ice sheet area loss and retreat since the LIA maximum (1900 ± 13 C.E.) are 120 ± 16 km²/yr and 3.3 ± 0.7 m/yr, respectively. As with the horizontal retreat, these rates are averaged across the entire ice sheet.

Table 1 lists the results of the area loss, area loss rate, horizontal retreat, retreat rate, and associated errors. The data is given for each two-degree latitude bin in West and East Greenland, as well as the totals for West Greenland, East Greenland, and all Greenland. The uncorrected and corrected values discussed in Section 5.1 are listed. The corrected values are discussed in the text and displayed in the figures.

5.2.1 Area Loss

The land, lake, and marine zones represent the area of ice sheet loss since the LIA maximum, thus, the LIA area of the GrIS inland ice, corrected for mapping bias, was 13,327 ± 830 km² larger than its current extent. This area loss corresponds to 0.8% shrinkage of the GrIS inland ice. The total area loss captured along the West Greenland margin is 7,423 ± 461 km² and is 5,904 ± 370 km² along the East Greenland margin. In West Greenland the values of area loss in each latitude bin range from 86 ± 6 km² in 78 – 80 ˚N latitude to 1,818 ± 113 km² in 76 – 78 ˚N latitude. In East Greenland the values of area loss range from 304 ± 19 km² in 78 – 80 ˚N latitude to 791 ± 49 km² in 76 – 78 ˚N latitude (Table 1; Figure 7).

5.2.2 Horizontal Retreat

The horizontal retreat of the GrIS inland ice since the LIA averaged over the length of the ice sheet margin is 363 ± 69 m. The horizontal retreat in West Greenland is more than double the value in East Greenland. For West Greenland the averaged horizontal retreat is 560 ± 107 m and for East Greenland is 251 ± 48 m. In West Greenland the horizontal retreat values in each two-degree latitude bin range from 103 ± 20 m in 78 – 80 ˚N latitude to 1,485 ± 285 m in 74 – 76 ˚N latitude. In East Greenland the latitude bin retreat values range from 141 ± 27 m in 70 – 72 ˚N latitude to 598 ± 114 m in 64 – 66 ˚N latitude (Table 1; Figure 8). The bins with the greatest horizontal retreat include glaciers with large marine zones. In West Greenland latitude bin 74 – 76 ˚N, large marine zones are mapped near Hayes, Steenstrup, Nansen, Kong Oscar, and other unnamed glaciers that collectively contribute to the highest bin of horizontal retreat. The second highest horizontal retreat is measured in West Greenland latitude bin 68 – 70 ˚N predominantly from the 37-km frontal retreat of marine-terminating Jakobshavn Isbræ and its adjacent trimzones that are up to 9 km wide, the widest mapped in our study.

5.2.3 Rates of Area Loss and Retreat

The area loss values are divided by the estimated time since the LIA maximum (111 ± 13 years) to give averaged rates of area loss since the LIA maximum. For all of Greenland the averaged area loss rate is 120.1 ± 16.0 km²/yr. The West Greenland area loss rate is 66.9 ± 8.9 km²/yr and the East Greenland area loss rate is 53.2 ± 7.1 km²/yr. In West Greenland the area loss rate values range from 0.8 ± 0.1 km²/yr in 78 – 80 ˚N latitude to 16.4 ± 2.2 km²/yr in 76 – 78 ˚N latitude. In East Greenland the area loss rate values range from 2.7 ± 0.4 km²/yr in 78 – 80 ˚N latitude to 7.1 ± 0.9 km²/yr in 76 – 78 ˚N latitude (Table 1; Figure 9).

The horizontal retreat values are divided by the time since the LIA to give averaged rates of retreat since the LIA maximum. For all of Greenland the averaged retreat rate is 3.3 ± 0.7 m/yr. The West Greenland retreat rate (5.0 ± 1.1 m/yr) is faster than East Greenland (2.3 ± 0.5 m/yr). In West Greenland the retreat rate values range from 0.9 ± 0.2 m/yr in 78 – 80 ˚N latitude to 13.4 ± 3.0 m/yr in 74 – 76 ˚N latitude. In East Greenland the retreat rate values range from 1.3 ± 0.3 m/yr in 70 – 72 ˚N latitude to 5.4 ± 1.2 m/yr in 64 – 66 ˚N latitude (Table 1; Figure 9).

5.2.4 South Greenland Case Study of Shorter Term Area Loss and Retreat Rates: Methods and Results

Additional satellite scenes are downloaded for a region in South Greenland for the years 1992 and 2000 from the Landsat 5 and ASTER satellites, respectively, to supplement the 2012 Landsat 7 coverage. The selected area contains land-terminating ice margins separated by glaciers terminating in fjords connected to the Labrador Sea in the North Atlantic Ocean (Figure 4A). This area is selected because Landsat and ASTER satellite coverage is good at approximately decadal time steps (Figure 4D, 4E, 4F) and because recent ice sheet thinning has been observed in the region, but it has not experienced the greatest changes seen elsewhere along the ice sheet periphery [*Krabill et al.*, 2004; *Bamber et al.*, 2007; *Sole et al.*, 2008; *Schenk and Csatho*, 2012; and others]. The trimzones at this portion of the GrIS margin mapped on the 2012 image are relatively wide and extend along the limbs of the fjords yielding mappable marine zones of area loss. Several lakes border the ice edge whose areas are surrounded by trimzones, hence the lakes are mapped as lake zones of area loss. Additionally, several nunataks near the inland ice edge contain trimzones whose areas are included in the area loss measurement (Figure 4F).

The position of the outer trimzone boundary mapped on the 2012 image (Figure 4F) is clearly observed in the same position on the

1992 and 2000 images (Figure 4D, 4E). To map the area loss on the 1992 and 2000 images, the original 2012 area loss polygons are copied and only the inner margins along the ice edges are edited to follow the 1992 and 2000 ice extents. The 2000 ice edge lies in front of the 2012 ice edge and the 1992 ice edge lies in front of the 2000 ice edge, each displaying ice margin retreat between the time periods (Figure 4B).

The total area loss value from the 1992 image represents the area loss that occurs between the LIA maximum and 1992. Such is the case for the total area loss values on the 2000 and 2012 images, so the total 1992 value is subtracted from the total 2000 value and the total 2000 value is subtracted from the total 2012 value to measure the area loss that occurs between each time period. These values are divided by the time elapsed between the acquisition dates of each satellite scene to yield the rates of ice sheet area loss that this region of the GrIS experiences (Figure 4C). From the LIA maximum to 1992 the area loss rate is 1.4 ± 0.2 km²/yr and accelerates to 2.6 ± 0.4 km²/yr for the time period 1992 to 2000. From 2000 to 2012 the area loss rate accelerates further to 3.6 ± 0.4 km²/yr.

The area loss measurements in this region cover a 174 km-long portion of the ice sheet margin. The area loss rates divided by the length of the margin yield retreat rates that can be compared to the rates measured along the rest of the ice sheet (Figure 4C). From the

LIA maximum to 1992 the South Greenland region retreats at a rate of 8.1 ± 1.9 m/yr. From 1992 to 2000 the retreat rate accelerates to 15.2 ± 3.5 m/yr. From 2000 to 2012 the retreat rate accelerates further to 20.7 ± 4.3 m/yr.

6 DISCUSSION

The data presented here elucidate the area change and change rates seen along different margin types (e.g., land-terminating versus marine-terminating margins) of the GrIS, as well as the ice sheet as a whole.

6.1 Land-Terminating and Marine-Terminating Margins

Our measurements for each two-degree latitude bin in West and East Greenland do not exhibit a clear latitudinal response of the GrIS retreat since the LIA (e.g., the more southerly latitudes do not experience greater ice sheet retreat than the northerly latitudes). Instead we find regional responses from larger geographic sections of the ice sheet margins that correspond to regions either dominated by land-terminating or marine-terminating margins. We separate the ice sheet into five quadrants, similar to those defined by *Weidick* [1995]. The SW quadrant encompasses West Greenland latitudes 60 – 72 ˚N, the NW quadrant encompasses West Greenland latitudes 72 – 78 ˚N, the North quadrant encompasses West and East Greenland latitudes 78 – 82 ˚N,

the NE quadrant encompasses East Greenland latitudes 70 – 78 ˚N, and the SE quadrant encompasses East Greenland latitudes 60 – 70 ˚N (Figure 1).

The SW is dominated by land-terminating margins but contains some marine-terminating glaciers that exhibit large retreat areas since the LIA. These marine-terminating glaciers include Sermilik Bræ, Qaleragdlit sermia, and others in 60 – 62 ˚N; Kangiata Nunâta Sermia in 64 – 66 ˚N; Jakobshavn Isbræ in 68 – 70 ˚N; and Umiámáko Isbræ in 70 – 72 ˚N. The area loss and retreat measurements of the SW latitude bins, when compared with the rest of the ice sheet, are moderate, except in latitude bin 68 – 70 ˚N that contains Jakobshavn Isbræ. Many studies report that Jakobshavn Isbræ has retreated the farthest and has the highest ice velocity of all Greenland glaciers [*Weidick*, 1995; *Csatho et al.*, 2008; *Joughin et al.*, 2008, 2014; and others]. We measure a ~ 37-km frontal retreat of Jakobshavn Isbræ since the LIA maximum and map trimzones up to 9 km wide on its adjacent land-terminating margins—the widest trimzones mapped in our study. Lake zones in the SW contribute relatively high zones of area loss when compared with the quantities of lake zones in the other latitude bins. As expected, lakes zones are more significant amongst the land-terminating sectors of the ice sheet, (e.g., the SW, North, and NE quadrants).

Marine-terminating glaciers dominate the NW. We measure large marine zones at Upernavik Isstrøm, Giesecke Bræer, and Ussing Bræer glaciers in latitude bin 72 – 74 ˚N; Hayes, Steenstrup, Nansen, Kong Oscar, and un-

named glaciers in latitude bin 74 – 76 ˚N; and Rink, Døcker Smith, Gade, Harald Moltke Bræ, Tracy, and other glaciers in latitude bin 76 – 78 ˚N. The area loss zones from these and other marine-terminating glaciers collectively make the NW the quadrant with the overall highest values of area loss and retreat.

The North quadrant of the GrIS margin is mostly land-terminating, except for a few of the largest marine-terminating glaciers on the island. We observe large zones of area loss attributed to Petermann Glacier in West Greenland latitude bin 80 – 82 ˚N. At least four large calving events of its floating ice tongue have been documented since the late 1950s, the largest of which (~ 270 km² in size) occurred in 2010 [*Johannessen et al.*, 2011]. Academy and Hagen Bræ glaciers in East Greenland latitude bin 80 – 82 ˚N also contribute significantly to the quadrant's area loss and retreat. Humboldt Glacier in West Greenland latitude bin 78 – 80 ˚N is the widest marine-terminating glacier on the island (110 km wide) and significant retreat of its margin in recent decades has been measured [*Box and Decker*, 2011]. However, our mapping of its retreat is limited because its calving front is not in contact with fjord walls, nor are smaller islands in its vicinity, thus Humboldt Glacier does not leave clear signatures of retreat on nearby coasts. Similarly, trimzones associated with the wide marine fronts of Nioghalvfjerdsbræ and Zachariae Isstrøm in East Greenland latitude bin 78 – 80 ˚N are limited, however other studies have measured retreating fronts, thinning, and increasing ice velocities of these

glaciers in recent decades [*Joughin et al.*, 2010; *Box and Decker*, 2011; *Khan et al.*, 2014]. Our measurements in West and East Greenland latitude bins 78 – 80 ˚N are likely underestimates.

The NE quadrant contains mostly land-terminating glaciers with low to moderate area loss and retreat. Latitude bin 76 – 78 ˚N contains the large marine-terminating glaciers Kofoed-Hansen Bræ, Storstrømmen, and L. Bistrup Bræ whose retreats significantly contribute to the bin's area loss. As with the SW quadrant, the NE includes measurable lake zones of area loss amongst its land-terminating margins.

Glaciers in the SE quadrant are mostly marine-terminating. Retreat of Kangerdlugssuaq and Helheim glaciers in latitude bins 68 – 70 ˚N and 66 – 68 ˚N, respectively, contribute the most to our measured area loss in each bin. These glaciers along with the area loss of numerous marine-terminating glaciers in the remainder of the SE bins collectively make the quadrant's area loss and retreat values moderate to high, especially the retreat of glaciers flowing into Gyldenlove Fjord and Køge Bugt in 64 – 66 ˚N. In the SE and NW quadrants, lake zones of area loss are not significant contributors to the quadrants' area losses.

Other studies have compared changes of land- versus marine-terminating Greenland glaciers since the 1970s and find small change along land-terminating margins but very high rates of change of many marine-terminating glaciers [*Moon and Joughin*, 2008; *Sole et al.*, 2008]. Our area

loss measurements are consistent with these studies. The latitude bins that encompass mostly land-terminating glaciers comprise the lowest area loss measurements, except where the measurements are skewed by few local marine-terminating glaciers. The quadrants that contain mostly marine-terminating margins have the highest area loss and retreat measurements.

When comparing our measurements to other studies of ice sheet velocities and rates of elevation change, we find that the bins with the largest area loss and retreat correspond to the fastest velocities and greatest thinning measured along the ice sheet margins, which are the regions dominated by marine-terminating outlets [*Rignot and Mouginot*, 2012; *Pritchard et al.*, 2009]. It is important to note that we are comparing ice sheet processes that differ from what we measured but find a correlation. In Figure 10 we display our area loss and retreat measurements next to maps of ice sheet velocities (how fast the ice flows) and elevation change rates (the rates of inflation and deflation of the ice sheet surface) to show the correlation. For example, in Figure 10A the *Rignot and Mouginot* [2012] ice velocity map shows two large regions in central West and NW Greenland of fast velocities that stretch relatively far into the ice sheet interior. These regions are approximately between 68 – 70 ˚N and 72 – 78 ˚N, which are mostly composed of marine-terminating glaciers including Jakobshavn Isbræ in 68 – 70 ˚N. These regions correspond to the four latitude bins in West Greenland with the largest area loss, especially marine, and retreat measurements. The faster velocities of Petermann (West

Greenland latitude bin 80 – 82 ˚N), Storstrømmen (East Greenland latitude bin 76 – 78 ˚N), and Kangerdlugssuaq (East Greenland latitude bin 68 – 70 ˚N) glaciers, as well as the marine-terminating outlets that make up the SE latitude bins from 60 – 68 ˚N, are also captured in our high area loss and retreat measurements in those bins. However, due to our mapping limitations near Humboldt (West Greenland latitude bin 78 – 80 ˚N), Nioghalvfjerdsbræ, and Zachariae Isstrøm (East Greenland latitude bin 78 – 80 ˚N) glaciers, the fast velocities of these glaciers are not captured in our measurements. Another correlation exists between the smaller area loss and retreat measurements along the land-terminating margins that correspond to the areas of slower ice sheet margin velocities (e.g., West Greenland latitude bins 62 – 68 ˚N and East Greenland latitude bins 70 – 76 ˚N). The *Pritchard et al.* [2009] ice elevation change map in Figure 10B illustrates that the greatest ice sheet thinning occurs near Jakobshavn Isbræ and along the margins in the NW and SE quadrants, which each correspond to larger area loss and retreat measurements in West Greenland latitude bins 68 – 70 ˚N and 72 – 78 ˚N, and East Greenland latitude bins 60 – 70 ˚N, respectively.

Many studies have focused on the processes responsible for the substantial changes of the marine-terminating glaciers that the land-terminating margins have not expressed as rapidly (e.g., *Moon and Joughin* [2008], *Sole et al.* [2008], *Zwally et al.* [2011], and others). Understanding uncertainties surrounding rapid glacial thinning and retreat are imperative when trying to

quantify and predict near future responses of the ice sheet to further warming conditions. Many of the uncertainties lie in the feedbacks pertaining to dynamic thinning of the margins. Dynamic thinning includes processes like accelerated glacial flow velocities due to increased meltwater lubrication of the bed [*Zwally et al.*, 2002]; increased driving stresses due to more steeply inclined, retreating glacial fronts [*Howat et al.*, 2005]; and increased calving and basal thinning of outlet glaciers in contact with warming ocean waters [*Holland et al.*, 2008]. *Sole et al.* [2008] find that 70% of marine- and 10% of land-terminating marginal thinning can be attributed to dynamical responses, thus although ice dynamics affect marine-terminating glaciers substantially more than land-terminating margins, the land-terminating margins still express ice-dynamical changes. Contrarily, *Tedstone et al.* [2013] report that land-terminating margins are not susceptible to increases in flow velocity due to increased summer surface meltwater percolating to the base. With the information reported by *Sole et al.* [2008] and *Tedstone et al.* [2013], we postulate that change seen along land-terminating margins is more indicative of long-term regional climatic changes.

6.2 Area Change and Rates of Change

In order to place our century-scale, high resolution GrIS area change measurements in context with more recently measured changes, we compare our data to similar studies of ice area change over the satellite observation pe-

riod. Based on collections of aerial photography from 1978 and 1987, *Citterio and Ahlstrøm* [2013] measure the total glacierized area of Greenland to be 1,804,638 ± 2,178 km² of which 88,083 ± 1,240 km² belongs to local glaciers and ice caps. The total area of local glaciers and ice caps includes 67,143 ± 1,057 km² of ice masses that are completely separate from the GrIS. We believe the area of the GrIS for which we conduct area loss studies is similar to the glacierized area without the separate ice masses but includes attached local glaciers, which is 1,737,495 km². Our measured area loss of 13,327 ± 830 km² equates to 0.8% reduction in the surface area of the GrIS since the LIA.

Kargel et al. [2012] compare preliminary versions of the *Citterio and Ahlstrøm* [2013] area data adjusted to ice margins from 2011 NASA LANCE Rapid Response MODIS imagery. They find an area loss of 2,560 ± 260 km² corresponding to an area loss rate of ~ 92 km²/yr since the 1980s. We find a faster rate of area loss since the LIA, 120.1 ± 16.0 km²/yr, especially when considering that the *Kargel et al.* [2012] study includes area loss of ice masses that we do not include in our analysis. However, *Kargel et al.* [2012] exclude known glacier surges that may account for a significant portion of our results. Although we did not distinguish the area loss from surging outlets during our data collection, we can assume that the surges they refer to likely occurred in marine-terminating outlets. Our marine zones of area loss make up more than half of our total area loss measurements. We do not claim that all marine area loss is excluded from the *Kargel et al.* [2012] area loss study but acknowledge

its potentially large effect on our area loss rate measurement of 120.1 ± 16.0 km²/yr. Furthermore, the slower area loss rate from *Kargel et al.* [2012] could be influenced by the relatively large MODIS pixel size (250 m) used to map the 2011 ice sheet margin. The larger pixel size would not capture the area loss zones we are able to map on the 30-m spatial resolution Landsat imagery.

Further comparisons to late 20th- to 21st-century GrIS margin change are performed with studies that focus on marine-terminating glaciers. *Box and Decker* [2011] measure area losses for 39 of Greenland's widest marine-terminating glaciers in the 2000-2010 decade, which include the 2010 Petermann Glacier calving event. These glaciers account for a total area loss of 1,368 km² over 10 years [*Box and Decker*, 2011]. Although this is not a long-term dataset, the area loss rate of the 39 marine-terminating glaciers alone (136.8 km²/yr) is greater than our ice sheet wide area loss rate since the LIA.

Howat and Eddy [2011] measure increasing rates of frontal retreat for subsets of 210 marine-terminating glaciers during the time periods 1972 to 1985 (mean retreat of 15 m/yr), 1985 to 2000 (mean retreat of 22 m/yr), and 2000 to 2010 (mean retreat of 110 m/yr). The fastest retreat rate we measure (13.4 ± 3.0 m/yr) is in West Greenland latitude bin 74 – 76 ˚N. This region is dominated by marine-terminating outlet glaciers and has a retreat rate comparable to the *Howat and Eddy* [2011] 1972-1985 mean rate for their subset of 105 glaciers. Therefore, our fastest century-scale retreat rate is comparable to the retreat rate of marine outlet glaciers seen during the 1970s and 1980s.

Taken in context with the climate conditions of the time, although *Howat and Eddy* [2011] report a net retreat rate of 15 m/yr, the measured 1972-1985 glacier changes follow a 60-year cooling period that ushered the advance of some glaciers. Further, *Box and Colgan* [2013] report that the period 1972 to 1998 corresponds to a positive mass balance of the ice sheet, likely in response to the mid-20th century cooling. The signature of the positive mass balance is also seen in the moderate retreat rate *Howat and Eddy* [2011] report for the 1985-2000 period. Thus, marine-terminating outlets still exhibit net retreat amidst late 20th-century cooling and accelerate vastly in the most recent decade, which is consistent with *Box and Decker* [2011]. The rates measured for the most recent decade are an order of magnitude faster than our century-scale, ice sheet-wide rate.

We observe increasing rates of change along the subset of mixed marine- and land-terminating South Greenland ice sheet margin that we measure for the time periods LIA maximum to 1992 (8.1 ± 1.9 m/yr), 1992 to 2000 (15.2 ± 3.5 m/yr), and 2000 to 2012 (20.7 ± 4.3 m/yr). Our data is consistent with the acceleration *Howat and Eddy* [2011] measure, even though it does not represent the greatest changes seen elsewhere across the ice sheet margins.

While the *Kargel et al.* [2012] dataset is a conservative, albeit similar, dataset to compare to, data solely of marine-terminating outlets offer information that represent the largest, fastest, and most variable marginal changes not dampened by smaller changes seen along the land-terminating margins.

Results from our study are comparable to the ice-sheet wide area loss study, but, as expected, are much smaller than the marine-terminating glacier change studies from the late 20th to 21st centuries.

7 CONCLUSION

We measure 0.8% shrinkage of the GrIS inland ice since the LIA, an area loss of 13,327 ± 830 km². The areas of greatest retreat are along marine-terminating outlets, especially in the NW. Land-terminating margins exhibit measureable retreat in the century since the LIA maximum and it is important to consider their effect in dampening the ice sheet-wide area loss rates. Furthermore, the GrIS margins exhibit a lagged response to changing temperatures on the order of a decade, suggesting that the unprecedented 2000-2010 retreat of the GrIS margins is in response to late 20th-century warming. The most recent decade has experienced further warming, especially in the high latitudes [*IPCC*, 2013], hence near future retreat of the GrIS could continue at its unprecedented rate. However, we find that recent decadal rates of change are higher than the century-scale average determined in our study.

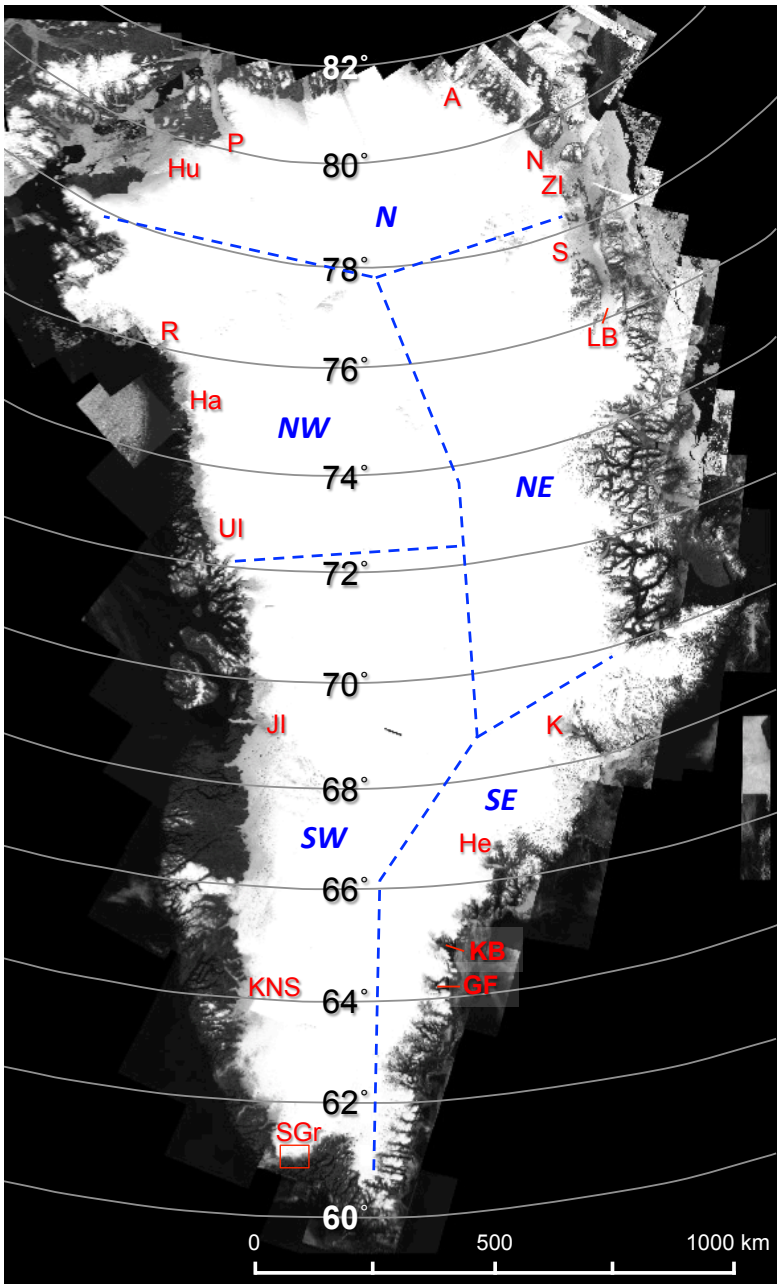

Figure 1: Regional map of Greenland divided into two-degree latitude bins and five quadrants. Background image is a mosaic of Landsat 7 images compiled by the University of New Hampshire EOS. Red letters are the following: "SGr"=South Greenland case study, "KNS"=Kangia Nunâta sermia, "JI"=Jakobshavn Isbræ, "UI"=Upernavik Isstrøm, "Ha"=Hayes Gletscher, "R"=Rink Gletscher, "Hu"=Humboldt Gletscher, "P"= Petermann Gletscher, "A"=Academy Gletscher, "N"=Nioghalvfjerdsbræ, "ZI"=Zachariae Isstrøm, "S"=Storstrømmen, "LB"=L. Bistrup Bræ, "K"=Kangerdlugssuaq, "He"=Helheim, "KB"=Køge Bugt, "GF"= Gyldenløve Fjord.

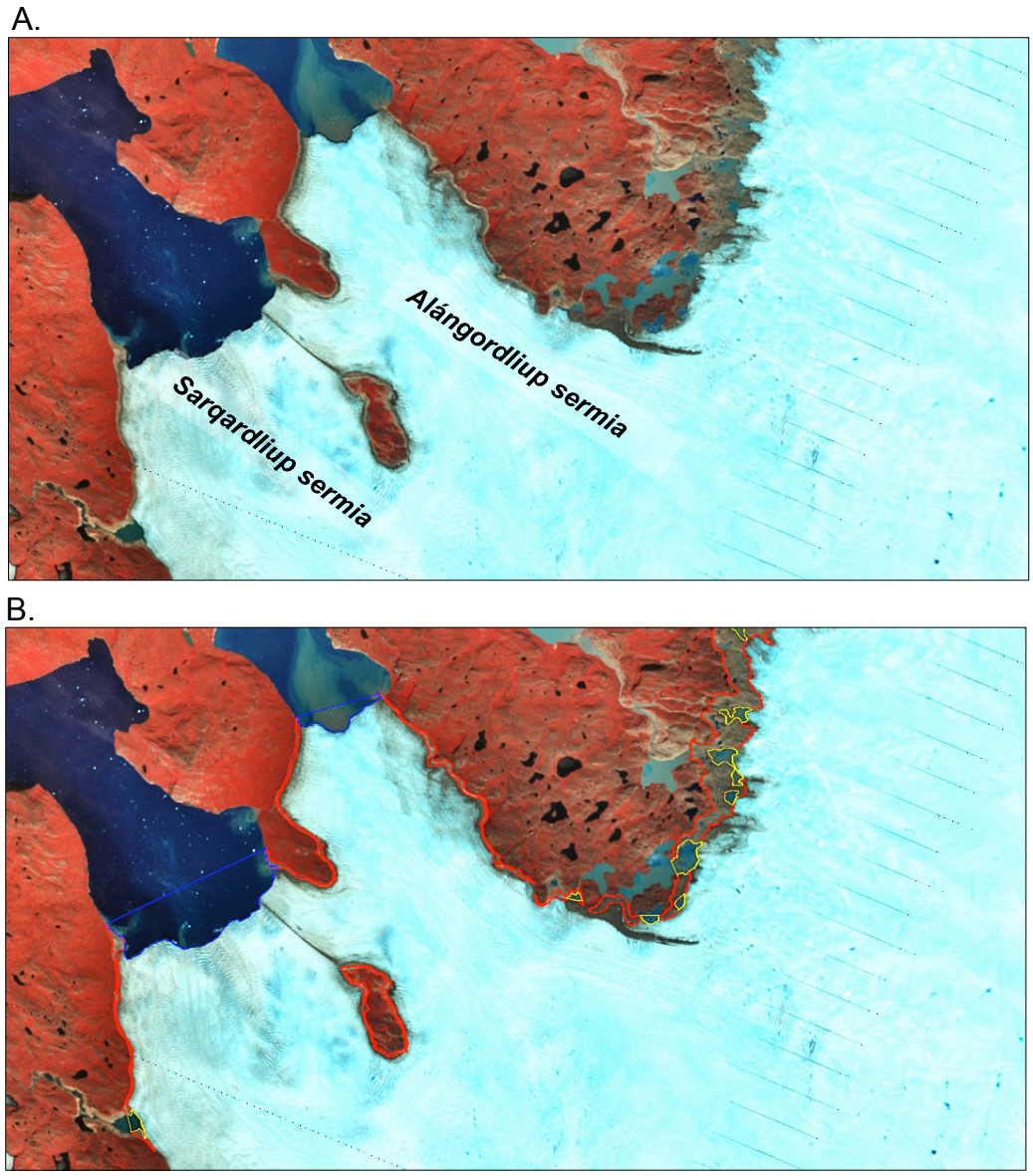

Figure 2: Trimzone mapping example. **(A.)** Visible near-infrared (VNIR) false color display of Sarqardliup sermia and Alángordliup sermia (south of Jakobshavn Isbræ) without trimzone mapping. **(B.)** Trimzone (red), lake (yellow), and marine (blue) zones of area loss mapped.

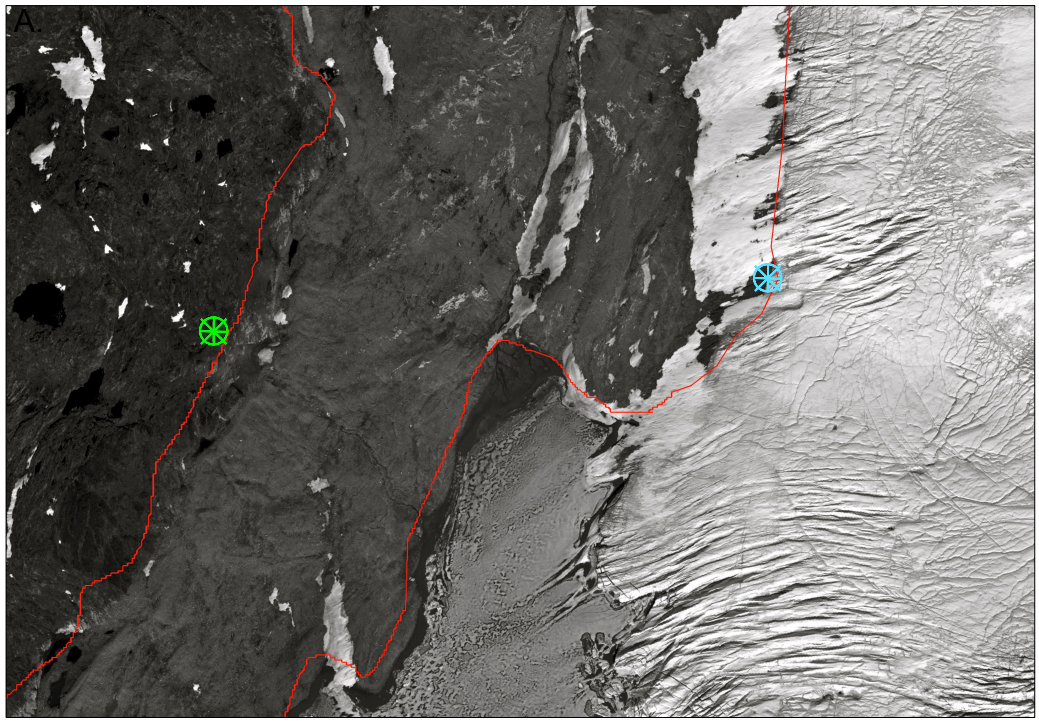

Figure 3: Example of trimzone mapping corrections. The image is a 0.5-m resolution panchromatic band WorldView mosaic of central West Greenland (north of Jakobshavn Isbræ). Landsat-mapped trimzones are overlain in red. The green-circled asterisk is a field-mapped GPS point of the outer trimline. The light blue-circled asterisk is a WorldView-mapped ice edge location.

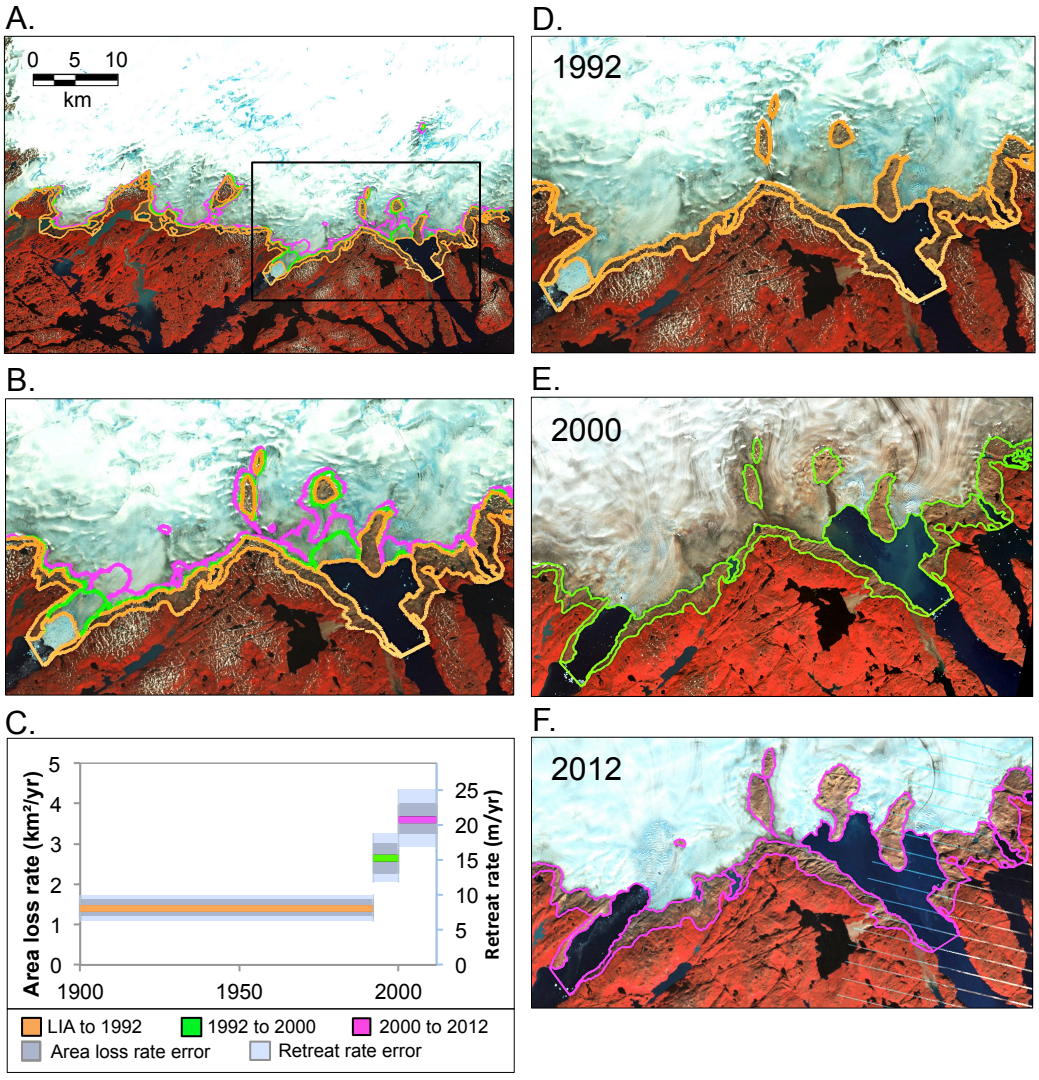

Figure 4: South Greenland case study. **(A.)** 1992 Landsat 5 image showing all 1992, 2000, and 2012 area loss zones included in the case study. **(B.)** Close-up of area in black box on (A.) with 1992, 2000, and 2012 area loss zones. **(C.)** Graph of area loss and retreat rates. **(D.)** Close-up of 1992 Landsat 5 image with 1992 area loss zones. **(E.)** Close-up of 2000 ASTER image with 2000 area loss zones. **(F.)** Close-up of 2012 Landsat 7 image with 2012 area loss zones.

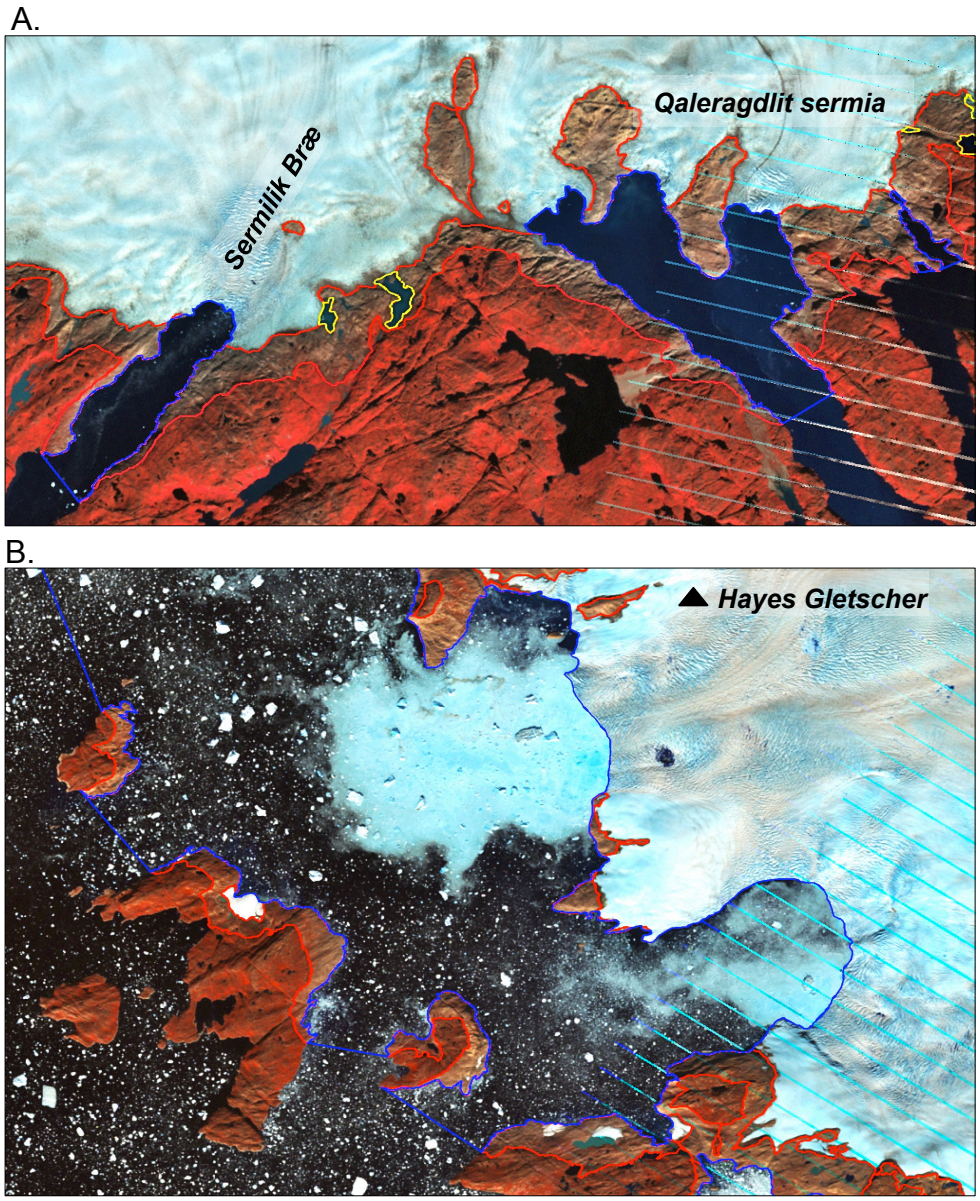

Figure 5: Examples of marine zones of area loss, mapped in blue. **(A.)** Sermilik Bræ and Qaleragdlit sermia glaciers in South Greenland terminating in ocean-connected fjords. Trimzones on the fjord walls indicate the LIA extent of the glaciers in the fjords. **(B.)** Unnamed glaciers south of Hayes Gletscher in NW Greenland with trimzones on nearby islands indicating the LIA extent of the marine-terminating glaciers.

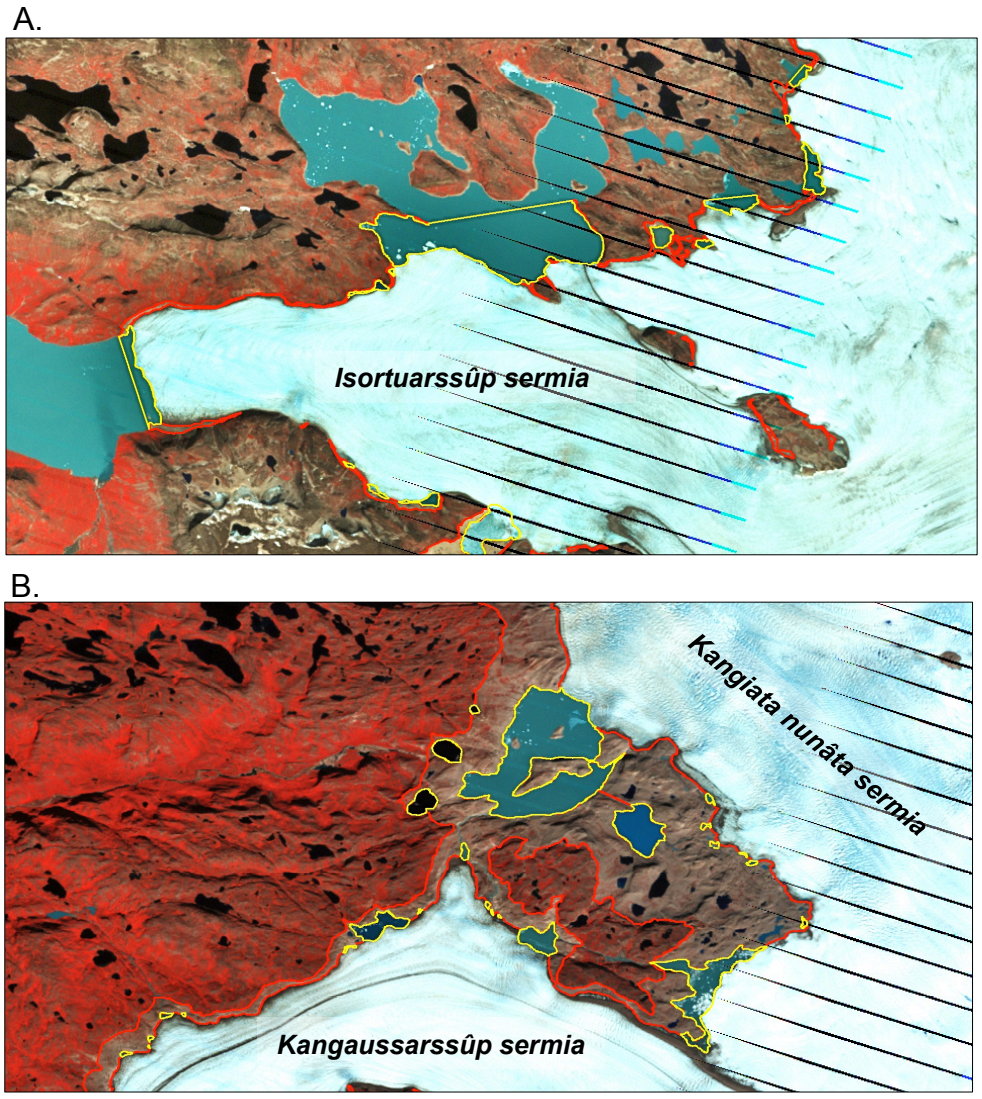

Figure 6: Examples of lake zones of area loss, mapped in yellow. **(A.)** Isortuarssûp sermia glacier in SW Greenland with lake-terminating margins. Trim-zones along lake edges indicate the LIA extent of the glacier that at least partially covered the present-day lake. **(B.)** Lakes surrounded by trimzones between Kangiata nunâta sermia and Kangaussarssûp sermia glaciers in SW Greenland indicating the LIA extent of the glaciers that are now lakes.

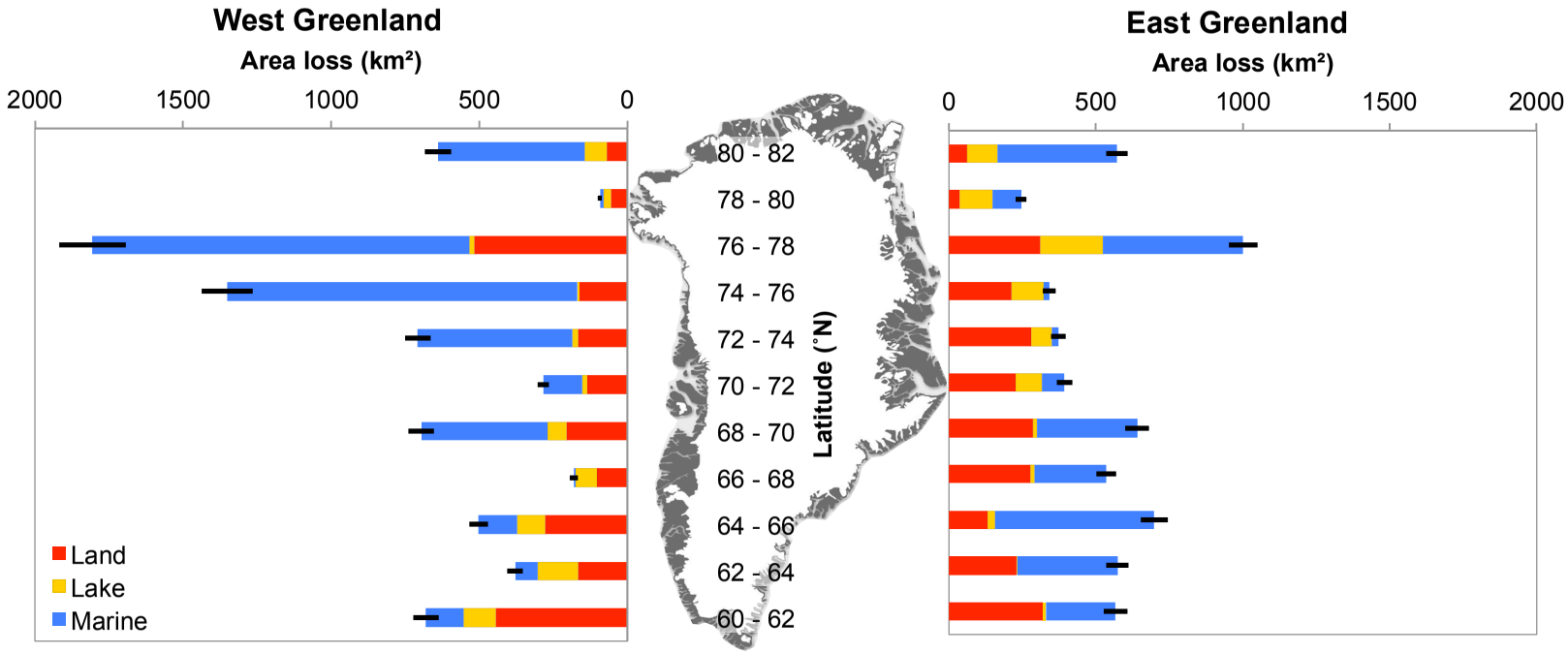

Figure 7: Graphs of area loss separated into land/trimzone (red), lake (yellow), and marine (blue) zones per two-degree latitude bin in West and East Greenland. Error bars are displayed as black lines. A Greenland map is shown for spatial reference.

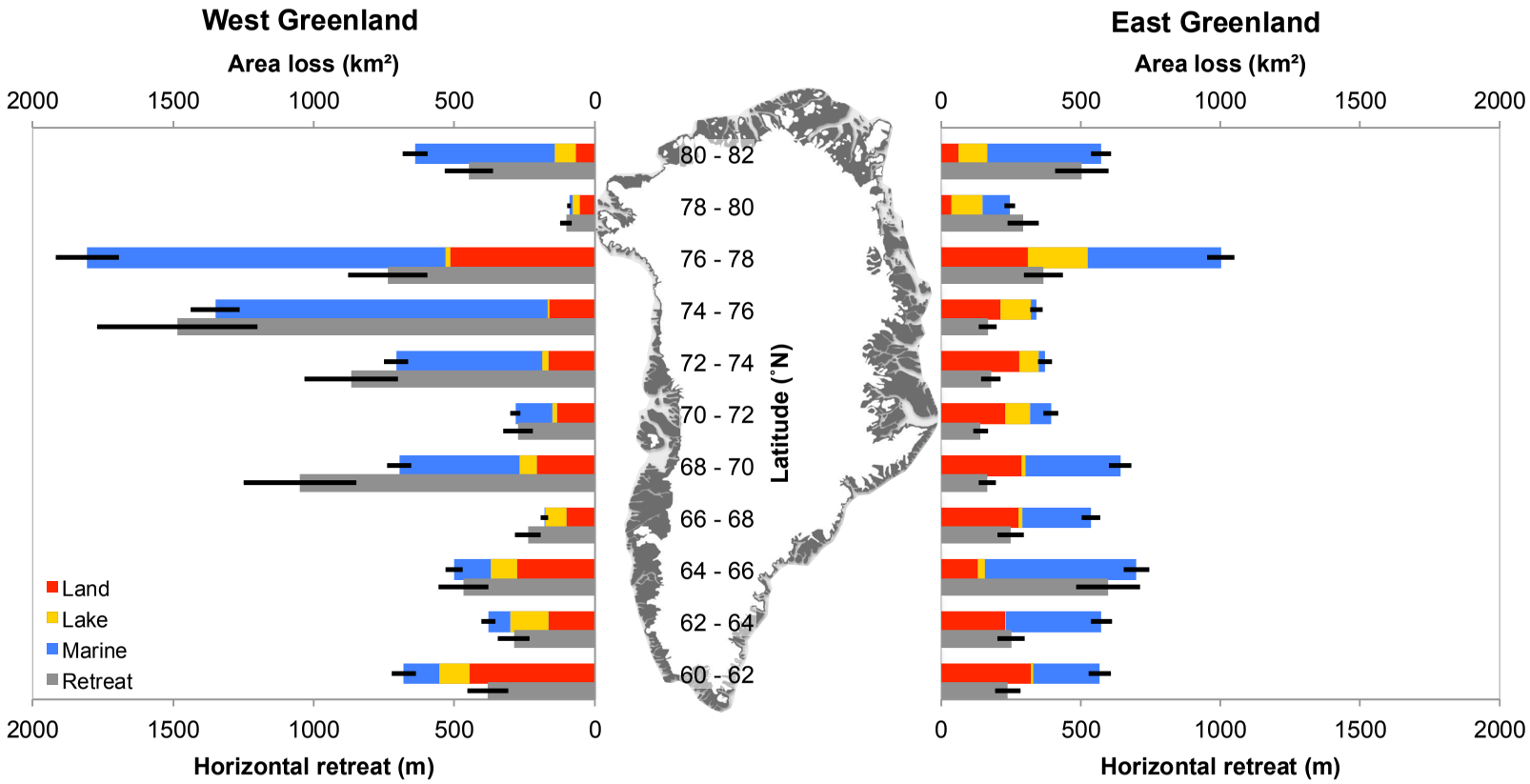

Figure 8: Graphs of area loss separated into land/trimzone (red), lake (yellow), and marine (blue) zones, as well as horizontal retreat (gray) per two-degree latitude bin in West and East Greenland. Error bars are displayed as black lines. A Greenland map is shown for spatial reference.

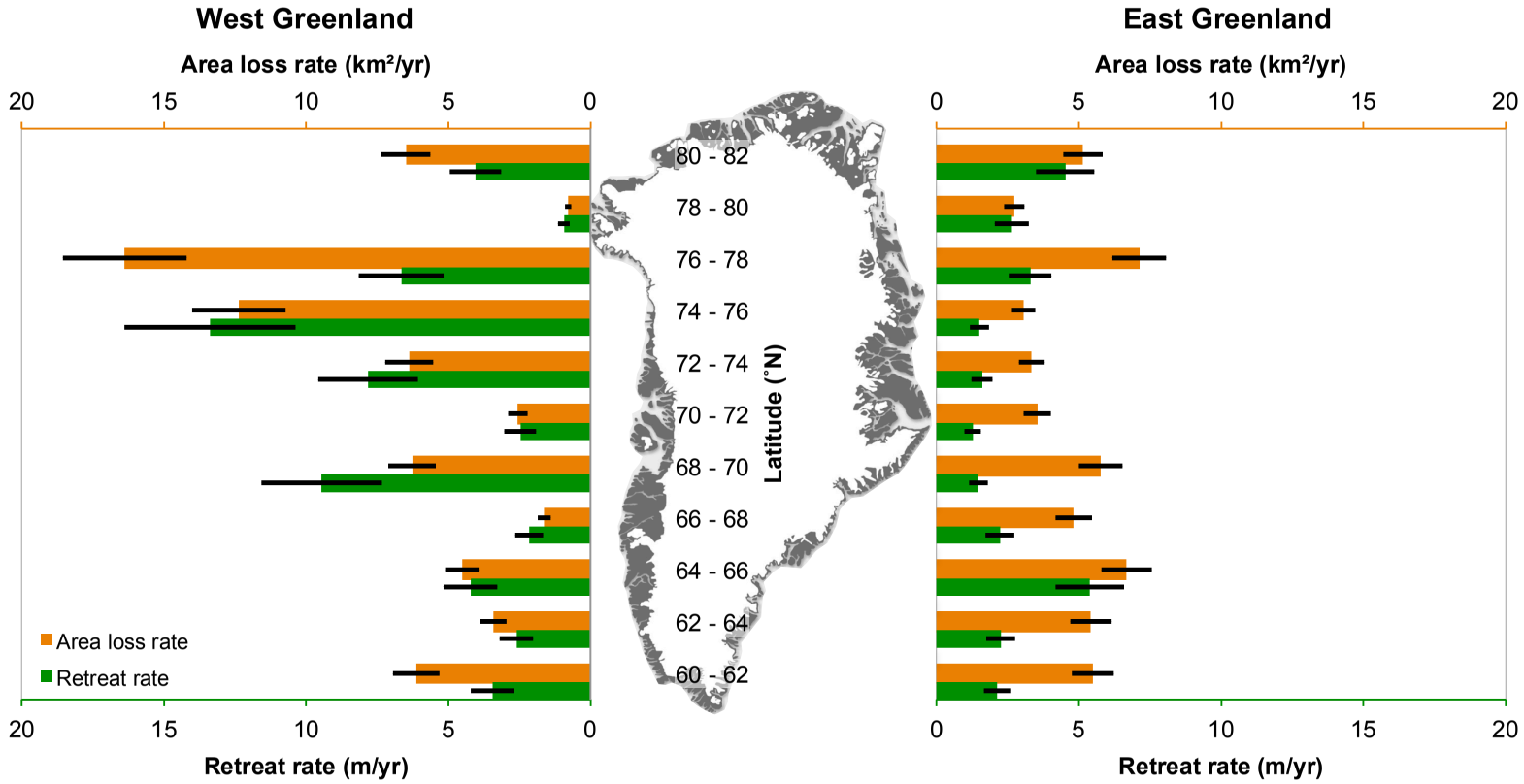

Figure 9: Graphs of area loss rate (orange) and retreat rate (green) per two-degree latitude bin in West and East Greenland. Error bars are displayed as black lines. A Greenland map is shown for spatial reference.

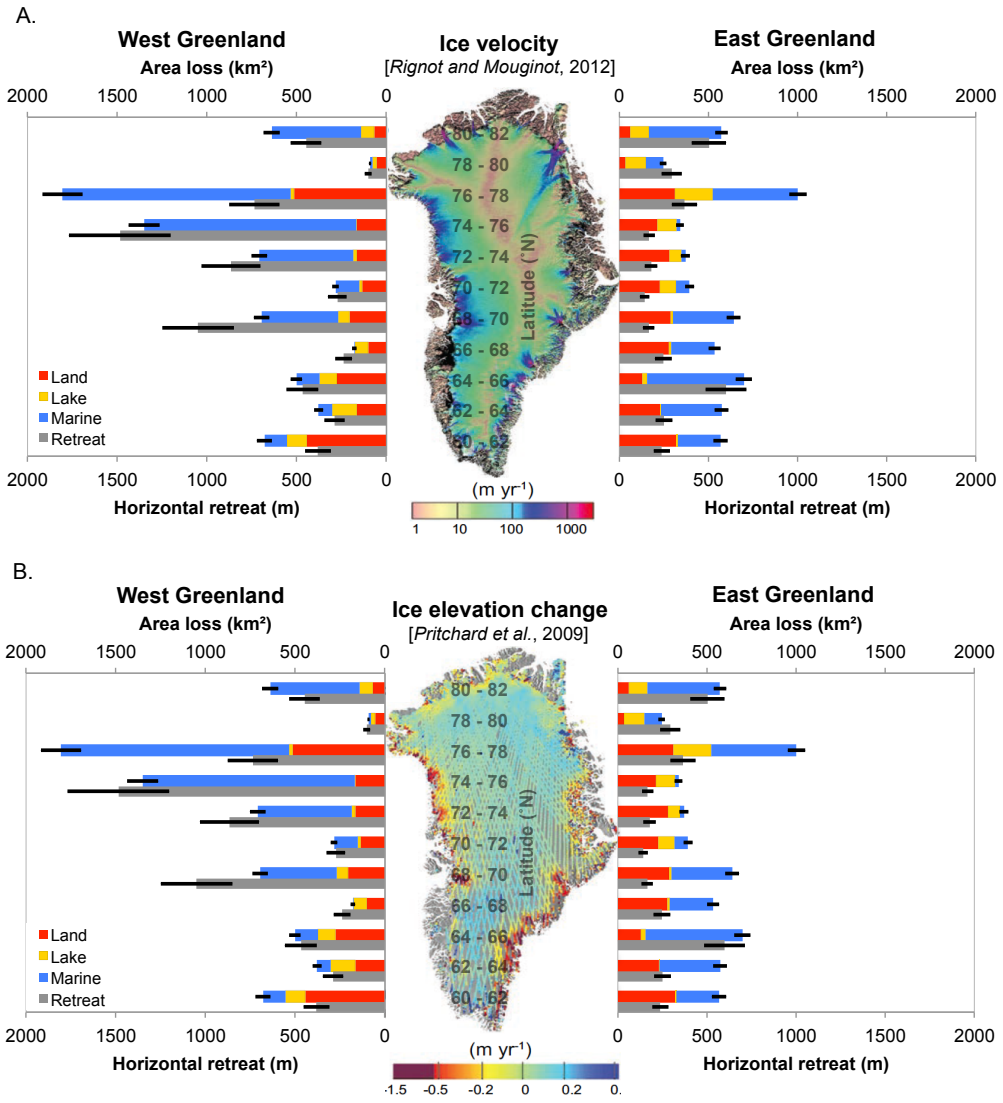

Figure 10: Graphs of area loss separated into land/trimzone (red), lake (yellow), and marine (blue) zones, as well as horizontal retreat (gray) per two-degree latitude bin in West and East Greenland. Error bars are displayed as black lines. **(A.)** With ice velocity map from *Rignot and Mouginot*, [2012] for comparison. **(B.)** With ice elevation change map from *Prichard et al.*, [2009] for comparison.

Table 1: Greenland Ice Sheet area loss, retreat, and rate measurements

	Latitude (°N)	Area loss						Rate of area loss			Horizontal retreat			Rate of retreat		
		Uncorrected (km²)				Corrected (km²)	Uncertainty (km²)	Uncorrected (km²/yr)	Corrected (km²/yr)	Uncertainty (km²/yr)	Uncorrected (m)	Corrected (m)	Uncertainty (m)	Uncorrected (m/yr)	Corrected (m/yr)	Uncertainty (m/yr)
		Land	Lake	Marine	Total											
West Greenland	60 - 62	360	88	102	549	680	43	5.0	6.1	0.8	445	382	73	4.0	3.4	0.8
	62 - 64	122	99	56	276	379	26	2.5	3.4	0.5	304	289	56	2.7	2.6	0.6
	64 - 66	236	81	111	428	502	31	3.9	4.5	0.6	576	468	90	5.2	4.2	1.0
	66 - 68	70	51	3	124	180	13	1.1	1.6	0.2	238	239	47	2.1	2.2	0.5
	68 - 70	186	56	385	627	696	43	5.6	6.3	0.8	1,365	1,050	201	12.3	9.5	2.1
	70 - 72	105	15	101	220	283	18	2.0	2.6	0.3	307	274	53	2.8	2.5	0.6
	72 - 74	146	19	460	625	707	44	5.6	6.4	0.8	1,105	866	166	10.0	7.8	1.8
	74 - 76	175	4	1,116	1,295	1,371	87	11.7	12.4	1.6	2,024	1,485	285	18.2	13.4	3.0
	76 - 78	465	16	1,123	1,604	1,818	113	14.4	16.4	2.2	939	737	140	8.5	6.6	1.5
	78 - 80	33	18	9	59	86	6	0.5	0.8	0.1	102	103	20	0.9	0.9	0.2
	80 - 82	135	69	451	655	720	45	5.9	6.5	0.9	589	449	86	5.3	4.0	0.9
	60 - 82	*2,032*	*514*	*3,917*	*6,464*	*7,423*	*461*	*58.2*	*66.9*	*8.9*	*703*	*560*	*107*	*6.3*	*5.0*	*1.1*
East Greenland	60 - 62	279	7	183	469	610	40	4.2	5.5	0.7	265	238	46	2.4	2.1	0.5
	62 - 64	211	2	277	491	603	38	4.4	5.4	0.7	294	251	48	2.7	2.3	0.5
	64 - 66	156	23	489	668	742	46	6.0	6.7	0.9	777	598	114	7.0	5.4	1.2
	66 - 68	226	11	199	437	535	34	3.9	4.8	0.6	292	248	48	2.6	2.2	0.5
	68 - 70	246	13	292	551	641	40	5.0	5.8	0.8	204	165	32	1.8	1.5	0.3
	70 - 72	170	67	57	294	394	26	2.6	3.5	0.5	152	141	27	1.4	1.3	0.3
	72 - 74	205	50	16	272	372	25	2.4	3.3	0.5	188	178	35	1.7	1.6	0.4
	74 - 76	164	83	15	261	341	22	2.4	3.1	0.4	185	167	32	1.7	1.5	0.3
	76 - 78	88	189	422	699	791	49	6.3	7.1	0.9	467	366	70	4.2	3.3	0.7
	78 - 80	81	99	84	264	304	19	2.4	2.7	0.4	368	294	56	3.3	2.7	0.6
	80 - 82	57	94	374	526	572	36	4.7	5.2	0.7	666	503	96	6.0	4.5	1.0
	60 - 82	*1,885*	*637*	*2,408*	*4,931*	*5,904*	*370*	*44.4*	*53.2*	*7.1*	*303*	*251*	*48*	*2.7*	*2.3*	*0.5*
All Greenland		*3,918*	*1,151*	*6,325*	*11,394*	*13,327*	*830*	*102.7*	*120.1*	*16.0*	*447*	*363*	*69*	*4.0*	*3.3*	*0.7*

Table 1: Greenland Ice Sheet area loss, area loss rate, horizontal retreat, and retreat rate measurements with associated measurement uncertainty. Area loss measurements are divided into land (trimzone), lake, and marine zones. The data is given for each two-degree latitude bin in West and East Greenland, as well as the totals for West Greenland, East Greenland, and all Greenland. Refer to Section 5.1 for a description of the uncorrected and corrected measurement values and determination of uncertainty.

Table 2: Inventory of images

Sensor	Image Name	Date (YYYY-MM-DD)	West or East	Latitude bin
Landsat 7	LE70010052012211EDC00	2012-07-29	E	76-78
Landsat 7	LE70010062012227EDC00	2012-08-14	E	74-76, 76-78
Landsat 7	LE70010142012227EDC00	2012-08-14	E	64-66
Landsat 7	LE70010152012227EDC00	2012-08-14	E	62-64, 64-66
Landsat 7	LE70010162012179ASN00	2012-06-27	E	62-64
Landsat 7	LE70010162012227EDC00	2012-08-14	E	62-64
Landsat 7	LE70010172012179ASN00	2012-06-27	E	60-62, 62-64
Landsat 7	LE70010172012195ASN00	2012-07-13	W & E	60-62, 62-64
Landsat 7	LE70010172012227ASN00	2012-08-14	W & E	60-62, 62-64
Landsat 7	LE70020042010212ASN00	2010-07-31	E	76-78, 78-80
Landsat 7	LE70020052010212ASN00	2010-07-31	E	76-78
Landsat 7	LE70020062011215EDC00	2011-08-03	E	74-76, 76-78
Landsat 7	LE70020172012202ASN00	2012-07-20	W	60-62; SGr
Landsat 7	LE70020172012250ASN00	2012-09-06	W	60-62; SGr
Landsat 7	LE70030042012209ASN00	2012-07-27	E	76-78, 78-80
Landsat 7	LE70030052012209EDC00	2012-07-27	E	76-78
Landsat 7	LE70030172011222EDC00	2011-08-11	W	60-62
Landsat 7	LE70030172012225EDC00	2012-08-12	W	60-62
Landsat 7	LE70040042010194ASN00	2010-07-13	E	76-78, 78-80
Landsat 7	LE70040052010194ASN00	2010-07-13	E	76-78
Landsat 7	LE70040162011181ASN00	2011-06-30	W	60-62, 62-64
Landsat 7	LE70040162012200ASN00	2012-07-18	W	60-62, 62-64
Landsat 7	LE70040172012200ASN00	2012-07-18	W	60-62
Landsat 7	LE70040172012232EDC00	2012-08-19	W	60-62
Landsat 7	LE70050042011204EDC00	2011-07-23	E	76-78, 78-80
Landsat 7	LE70050052012191EDC00	2012-07-09	E	76-78
Landsat 7	LE70050152012207EDC00	2012-07-25	W	62-64, 64-66
Landsat 7	LE70050162010233EDC00	2010-08-21	W	60-62, 62-64
Landsat 7	LE70060042010208EDC00	2010-07-27	E	76-78, 78-80
Landsat 7	LE70060142012182EDC00	2012-06-30	W	64-66, 66-68
Landsat 7	LE70060152012198EDC00	2012-07-16	W	62-64, 64-66
Landsat 7	LE70070032007223EDC00	2007-08-11	E	78-80
Landsat 7	LE70070042012189EDC00	2012-07-07	E	76-78, 78-80
Landsat 7	LE70070132011234EDC00	2011-08-22	W	66-68
Landsat 7	LE70070142011234EDC00	2011-08-22	W	64-66, 66-68
Landsat 7	LE70070142012205EDC00	2012-07-23	W	64-66, 66-68
Landsat 7	LE70080032010190EDC00	2010-07-09	E	78-80
Landsat 7	LE70080122012164EDC00	2012-06-12	W	68-70, 70-72
Landsat 7	LE70080132011225EDC00	2011-08-13	W	66-68
Landsat 7	LE70080142011225EDC00	2011-08-13	W	64-66, 66-68
Landsat 7	LE70090032011200EDC00	2011-07-19	E	78-80
Landsat 7	LE70090112012171EDC00	2012-06-19	W	70-72
Landsat 7	LE70090122012171EDC00	2012-06-19	W	68-70, 70-72
Landsat 7	LE70100022009201EDC00	2009-07-20	E	78-80
Landsat 7	LE70100032009201EDC00	2009-07-20	E	78-80
Landsat 7	LE70100102012178ASN00	2012-06-26	W	70-72
Landsat 7	LE70100112012178ASN00	2012-06-26	W	70-72
Landsat 7	LE70110022011198EDC00	2011-07-17	E	78-80
Landsat 7	LE70110032011198EDC00	2011-07-17	E	78-80
Landsat 7	LE70110102011230EDC00	2011-08-18	W	70-72

Table 2: Inventory of images *(continued)*

Sensor	Image Name	Date (YYYY-MM-DD)	West or East	Latitude bin
Landsat 7	LE70110102012233EDC00	2012-08-20	W	70-72
Landsat 7	LE70120022012192ASN00	2012-07-10	E	78-80
Landsat 7	LE70120102012208ASN00	2012-07-26	W	70-72
Landsat 7	LE70120102012240EDC00	2012-08-27	W	70-72
Landsat 7	LE70120112012176ASN00	2012-06-24	W	70-72
Landsat 7	LE70130022011196ASN00	2011-07-15	E	78-80
Landsat 7	LE70130092012199EDC00	2012-07-17	W	70-72, 72-74
Landsat 7	LE70130092012215ASN00	2012-08-02	W	70-72, 72-74
Landsat 7	LE70130102012199EDC00	2012-07-17	W	70-72
Landsat 7	LE70140022007224EDC00	2007-08-12	E	78-80
Landsat 7	LE70140092010232ASN00	2010-08-20	W	70-72, 72-74
Landsat 7	LE70140092012190ASN00	2012-07-08	W	70-72, 72-74
Landsat 7	LE70150022010191ASN00	2010-07-10	E	78-80
Landsat 7	LE70150092011178EDC00	2011-06-27	W	70-72, 72-74
Landsat 7	LE70150092012165ASN00	2012-06-13	W	70-72, 72-74
Landsat 7	LE70160022010182EDC00	2010-07-01	E	78-80
Landsat 7	LE70160082011217EDC00	2011-08-05	W	72-74
Landsat 7	LE70170012011208EDC00	2011-07-27	E	80-82
Landsat 7	LE70170022011208EDC00	2011-07-27	E	78-80
Landsat 7	LE70170082009218EDC00	2009-08-06	W	72-74
Landsat 7	LE70170082010189ASN00	2010-07-08	W	72-74
Landsat 7	LE70170082012243ASN00	2012-08-30	W	72-74
Landsat 7	LE70180012011199EDC00	2011-07-18	E	80-82
Landsat 7	LE70180082009241EDC00	2009-08-29	W	72-74
Landsat 7	LE70180082011199EDC00	2011-07-18	W	72-74
Landsat 7	LE70190012012209ASN00	2012-07-27	E	80-82
Landsat 7	LE70190072009216EDC00	2009-08-04	W	74-76
Landsat 7	LE70190072009232EDC00	2009-08-20	W	74-76
Landsat 7	LE70200072010226EDC00	2010-08-14	W	74-76
Landsat 7	LE70200072012200ASA00	2012-07-18	W	74-76
Landsat 7	LE70210012010201EDC00	2010-07-20	E	80-82
Landsat 7	LE70210072011188ASN00	2011-07-07	W	74-76
Landsat 7	LE70210072012191ASA00	2012-07-09	W	74-76
Landsat 7	LE70220012011195EDC00	2011-07-14	E	80-82
Landsat 7	LE70220062012214ASN00	2012-08-01	W	74-76, 76-78
Landsat 7	LE70230062011218EDC00	2011-08-06	W	74-76, 76-78
Landsat 7	LE70240012010190ASN00	2010-07-09	E	80-82
Landsat 7	LE70240062010238EDC00	2010-08-26	W	74-76, 76-78
Landsat 7	LE70250012010181ASN00	2010-06-30	E	80-82
Landsat 7	LE70250012011184EDC00	2011-07-03	E	80-82
Landsat 7	LE70250062009194EDC00	2009-07-13	W	74-76, 76-78
Landsat 7	LE70260012009201ASN00	2009-07-20	E	80-82
Landsat 7	LE70260062011207EDC00	2011-07-26	W	74-76, 76-78
Landsat 7	LE70270012010179ASN00	2010-06-28	E	80-82
Landsat 7	LE70270062007235EDC00	2007-08-23	W	74-76, 76-78
Landsat 7	LE70280012012192ASN00	2012-07-10	E	80-82
Landsat 7	LE70280052011189ASN00	2011-07-08	W	76-78
Landsat 7	LE70280062011237ASN00	2011-08-25	W	74-76, 76-78
Landsat 7	LE70290052010209ASN00	2010-07-28	W	76-78
Landsat 7	LE70290052012183ASN00	2012-07-01	W	76-78

Table 2: Inventory of images *(continued)*

Sensor	Image Name	Date (YYYY-MM-DD)	West or East	Latitude bin
Landsat 7	LE70290062012183ASN00	2012-07-01	W	74-76, 76-78
Landsat 7	LE70300052009197EDC00	2009-07-16	W	76-78
Landsat 7	LE70300052012190ASN00	2012-07-08	W	76-78
Landsat 7	LE70300062010184ASN00	2010-07-03	W	74-76, 76-78
Landsat 7	LE70310012011194EDC00	2011-07-13	W	80-82
Landsat 7	LE70310052009204EDC00	2009-07-23	W	76-78
Landsat 7	LE70310052012197ASN00	2012-07-15	W	76-78
Landsat 7	LE70320012011201EDC00	2011-07-20	W	80-82
Landsat 7	LE70320042011185EDC00	2011-07-04	W	76-78, 78-80
Landsat 7	LE70320042012188ASN00	2012-07-06	W	76-78, 78-80
Landsat 7	LE70320052007222EDC00	2007-08-10	W	76-78
Landsat 7	LE70320052012188ASN00	2012-07-06	W	76-78
Landsat 7	LE70330012010189EDC01	2010-07-08	W	80-82
Landsat 7	LE70330032012211EDC00	2012-07-29	W	78-80
Landsat 7	LE70330042009202EDC00	2009-07-21	W	76-78, 78-80
Landsat 7	LE70330042010189EDC01	2010-07-08	W	76-78, 78-80
Landsat 7	LE70330052010189EDC01	2010-07-08	W	76-78
Landsat 7	LE70340012012186ASN00	2012-07-04	W	80-82
Landsat 7	LE70340012012202ASN00	2012-07-20	W	80-82
Landsat 7	LE70340022012202ASN00	2012-07-20	W	78-80, 80-82
Landsat 7	LE70340032012186ASN00	2012-07-04	W	78-80
Landsat 7	LE70340032012202ASN00	2012-07-20	W	78-80
Landsat 7	LE70340042011183EDC00	2011-07-02	W	76-78, 78-80
Landsat 7	LE70340042011199EDC00	2011-07-18	W	76-78, 78-80
Landsat 7	LE70340052011199EDC00	2011-07-18	W	76-78
Landsat 7	LE70350012011190EDC00	2011-07-09	W	80-82
Landsat 7	LE70350012012209ASN00	2012-07-27	W	80-82
Landsat 7	LE70350022011190EDC00	2011-07-09	W	78-80, 80-82
Landsat 7	LE70350032011190EDC00	2011-07-09	W	78-80
Landsat 7	LE70350042010187EDC00	2010-07-06	W	76-78, 78-80
Landsat 7	LE70360022012200ASN00	2012-07-18	W	78-80, 80-82
Landsat 7	LE70360032012200ASN00	2012-07-18	W	78-80
Landsat 7	LE70360042012184ASN00	2012-07-02	W	76-78, 78-80
Landsat 7	LE70360042012200ASN00	2012-07-18	W	76-78, 78-80
Landsat 7	LE70370022012191EDC00	2012-07-09	W	78-80, 80-82
Landsat 7	LE70370032012191EDC00	2012-07-09	W	78-80
Landsat 7	LE70370042011188EDC00	2011-07-07	W	76-78, 78-80
Landsat 7	LE70370042012191EDC00	2012-07-09	W	76-78, 78-80
Landsat 7	LE70380012011195EDC00	2011-07-14	W	80-82
Landsat 7	LE70380022011195EDC00	2011-07-14	W	78-80, 80-82
Landsat 7	LE70380022012198EDC00	2012-07-16	W	78-80, 80-82
Landsat 7	LE70380032012198EDC00	2012-07-16	W	78-80
Landsat 7	LE70390012010183EDC01	2010-07-02	W	80-82
Landsat 7	LE70390032011202EDC00	2011-07-21	W	78-80
Landsat 7	LE70400022012212ASN00	2012-07-30	W	78-80, 80-82
Landsat 7	LE70410012009194EDC00	2009-07-13	W	80-82
Landsat 7	LE70410022012187ASN00	2012-07-05	W	78-80, 80-82
Landsat 7	LE70420012009201EDC00	2009-07-20	W	80-82
Landsat 7	LE70430012010227EDC00	2010-08-15	W	80-82
Landsat 7	LE70430012012185ASN00	2012-07-03	W	80-82

Table 2: Inventory of images *(continued)*

Sensor	Image Name	Date (YYYY-MM-DD)	West or East	Latitude bin
Landsat 7	LE70440012011205EDC00	2011-07-24	W	80-82
Landsat 7	LE72250112012212EDC00	2012-07-30	E	68-70, 70-72
Landsat 7	LE72260102010213EDC00	2010-08-01	E	70-72
Landsat 7	LE72270102009201EDC00	2009-07-20	E	70-72
Landsat 7	LE72270102012226EDC00	2012-08-13	E	70-72
Landsat 7	LE72280102012217EDC00	2012-08-04	E	70-72
Landsat 7	LE72280112012217EDC00	2012-08-04	E	68-70, 70-72
Landsat 7	LE72280122010211EDC00	2010-07-30	E	66-68, 68-70
Landsat 7	LE72280122012217EDC00	2012-08-04	E	66-68, 68-70
Landsat 7	LE72290102012208EDC00	2012-07-26	E	70-72
Landsat 7	LE72290102012224EDC00	2012-08-11	E	70-72
Landsat 7	LE72290112012208EDC00	2012-07-26	E	68-70, 70-72
Landsat 7	LE72290122011221EDC00	2011-08-09	E	66-68, 68-70
Landsat 7	LE72290122012240ASN00	2012-08-27	E	66-68, 68-70
Landsat 7	LE72300082010225ASN00	2010-08-13	E	72-74
Landsat 7	LE72300082011196EDC00	2011-07-15	E	72-74
Landsat 7	LE72300092012231EDC00	2012-08-18	E	70-72, 72-74
Landsat 7	LE72300102012215EDC00	2012-08-02	E	70-72
Landsat 7	LE72300102012231EDC00	2012-08-18	E	70-72
Landsat 7	LE72300112012215EDC00	2012-08-02	E	68-70, 70-72
Landsat 7	LE72300112012231EDC00	2012-08-18	E	68-70, 70-72
Landsat 7	LE72300122012215EDC00	2012-08-02	E	66-68, 68-70
Landsat 7	LE72300122012231EDC00	2012-08-18	E	66-68, 68-70
Landsat 7	LE72300132012199EDC00	2012-07-17	E	64-66, 66-68
Landsat 7	LE72300132012215EDC00	2012-08-02	E	64-66, 66-68
Landsat 7	LE72310072011203EDC00	2011-07-22	E	74-76
Landsat 7	LE72310082011219EDC00	2011-08-07	E	72-74
Landsat 7	LE72310092011219EDC00	2011-08-07	E	70-72, 72-74
Landsat 7	LE72310102011203EDC00	2011-07-22	E	70-72
Landsat 7	LE72310102012206EDC00	2012-07-24	E	70-72
Landsat 7	LE72310122012190EDC00	2012-07-08	E	66-68, 68-70
Landsat 7	LE72310122012222EDC00	2012-08-09	E	66-68, 68-70
Landsat 7	LE72310132011219EDC00	2011-08-07	E	64-66, 66-68
Landsat 7	LE72310132012222EDC00	2012-08-09	E	64-66, 66-68
Landsat 7	LE72310142012222EDC00	2012-08-09	E	64-66
Landsat 7	LE72310142012254EDC00	2012-09-10	E	64-66
Landsat 7	LE72320062012213EDC00	2012-07-31	E	74-76, 76-78
Landsat 7	LE72320072012229EDC00	2012-08-16	E	74-76
Landsat 7	LE72320082012197EDC00	2012-07-15	E	72-74
Landsat 7	LE72320092012197EDC00	2012-07-15	E	70-72, 72-74
Landsat 7	LE72320092012213EDC00	2012-07-31	E	70-72, 72-74
Landsat 7	LE72320102012197EDC00	2012-07-15	E	70-72
Landsat 7	LE72320102012245EDC00	2012-09-01	E	70-72
Landsat 7	LE72320112012229EDC00	2012-08-16	E	68-70, 70-72
Landsat 7	LE72320112012245EDC00	2012-09-01	E	68-70, 70-72
Landsat 7	LE72320122012229EDC00	2012-08-16	E	66-68, 68-70
Landsat 7	LE72320122012245EDC00	2012-09-01	E	66-68, 68-70
Landsat 7	LE72320132012229EDC00	2012-08-16	E	64-66, 66-68
Landsat 7	LE72320132012245EDC00	2012-09-01	E	64-66, 66-68
Landsat 7	LE72320142012197EDC00	2012-07-15	E	64-66

Table 2: Inventory of images *(continued)*

Sensor	Image Name	Date (YYYY-MM-DD)	West or East	Latitude bin
Landsat 7	LE72320142012245EDC00	2012-09-01	E	64-66
Landsat 7	LE72320152012245EDC00	2012-09-01	E	62-64, 64-66
Landsat 7	LE72320162012197EDC00	2012-07-15	E	62-64
Landsat 7	LE72320162012245EDC00	2012-09-01	E	62-64
Landsat 7	LE72320172012245EDC00	2012-09-01	E	60-62, 62-64
Landsat 7	LE72320182012213EDC00	2012-07-31	E	60-62
Landsat 7	LE72320182012245EDC00	2012-09-01	E	60-62
Landsat 7	LE72330052011185EDC00	2011-07-04	E	76-78
Landsat 7	LE72330062011217EDC00	2011-08-05	E	74-76, 76-78
Landsat 7	LE72330072012220EDC00	2012-08-07	E	74-76
Landsat 7	LE72330082011217EDC00	2011-08-05	E	72-74
Landsat 7	LE72330132012172EDC00	2012-06-20	E	64-66, 66-68
Landsat 7	LE72330132012252EDC00	2012-09-08	E	64-66, 66-68
Landsat 7	LE72330142010214EDC00	2010-08-02	E	64-66
Landsat 7	LE72330142012204EDC00	2012-07-22	E	64-66
Landsat 7	LE72330152011217EDC00	2011-08-05	E	62-64, 64-66
Landsat 7	LE72330152012236EDC00	2012-08-23	E	62-64, 64-66
Landsat 7	LE72330152012252EDC00	2012-09-08	E	62-64, 64-66
Landsat 7	LE72330162012236EDC00	2012-08-23	E	62-64
Landsat 7	LE72330162012252EDC00	2012-09-08	E	62-64
Landsat 7	LE72330172011217EDC00	2011-08-05	E	60-62, 62-64
Landsat 7	LE72330172012236EDC00	2012-08-23	E	60-62, 62-64
Landsat 7	LE72330182009195EDC00	2009-07-14	W & E	60-62
Landsat 7	LE72330182011265EDC00	2011-09-22	W & E	60-62
Landsat 5	LT50020171992219PAC00	1992-08-06	W	60-62; SGr
ASTER	AST_L1B_00030812000145802	2000-08-11	W	60-62; SGr
WorldView	GreenlandMosaic_11_05_5_3	2009 - 2011	W	68-70; Ice edge correction

Table 2: Inventory of images used in this study. Satellite, image name, and date of image, are listed. Location of the image is indicated by West or East Greenland and its latitude bin (see Figure 1). Images with both West and East or two latitude bins indicated have coverage in each location. Images used in the South Greenland case study are indicated by "SGr." The WorldView image was used for the ice edge correction as part of our error analysis.

References

Alkan, M., G. Buyuksalih, U. G. Sefercik, and K. Jacobsen (2013), Geometric accuracy and information content of WorldView-1 images, *Opt. Eng.*, *52*(2), 026201, doi:10.1117/1.OE.52.2.026201.

Bamber, J. L., R. B. Alley, and I. Joughin (2007), Rapid response of modern day ice sheets to external forcing, *Earth Planet. Sc. Lett., 257*(1-2), 1-13, doi: 10.1016/j.epsl.2007.03.005.

Bamber, J. L., J. A. Griggs, R. T. W. L. Hurkmans, J. A. Dowdeswell, S. P. Gogineni, I. Howat, J. Mouginot, J. Paden, S. Palmer, E. Rignot, and D. Steinhage (2013), A new bed elevation dataset for Greenland, *The Cryosphere, 7*, 499-510, doi:10.5194/tc-7-499-2013.

Beschel, R. E., and A. Weidick (1973), Geobotanical and geomorphological reconnaissance in west Greenland, 1961, *Arct. Alp. Res., 5*(4), 311-319.

Blunden, J., and D. S. Arndt (2013), State of the Climate in 2012, *Bull. Amer. Meteor. Soc., 94*(8), S1–S238, doi:10.1175/2013BAMSStateoftheClimate.1.

Bjørk, A. A., K. H. Kjær, N. J. Korsgaard, S. A. Khan, K. K. Kjeldsen, C. S. Andresen, J. E. Box, N. K. Larsen, and S. Funder (2012), An aerial view of 80 years of climate-related glacier fluctuations in southeast Greenland, *Nat. Geosci., 5*(6), 427-432, doi:10.1038/ngeo1481.

Box, J. E., L. Yang, D. H. Bromwich, and L.-S. Bai (2009), Greenland Ice Sheet surface air temperature variability: 1840-2007, *J. Clim., (22)*14, 4029-4049, doi: 10.1175/2009/JCLI2816.1.

Box, J. E., and W. Colgan (2013), Greenland Ice Sheet Mass Balance Reconstruction. Part III: Marine Ice Loss and Total Mass Balance (1840-2010), *J. Clim., 26*(18), 6990-7002, doi:10.1175/JCLI-D-12-00546.1.

Box, J. E., and D. T. Decker (2011), Analysis of Greenland marine-terminating glacier area changes: 2000-2010, *Ann. Glaciol., 52*(59), 91-98.

Briner, J. P., H. A. M. Stewart, N. E. Young, W. Philipps, and S. Losee (2010), Using proglacial-threshold lakes to constrain fluctuations of the Jakobshavn Isbræ ice margin, western Greenland, during the Holocene, *Quat. Sci. Rev., 29*(27-28), 3861-3874, doi:10.1016/j.quascirev.2010.09.005.

Briner, J. P., N. E. Young, E. K. Thomas, H. A. M. Stewart, S. Losee, and S. Truex (2011), Varve and radiocarbon dating support the rapid advance of Jakobshavn Isbræ during the Little Ice Age, *Quat. Sci. Rev., 30*(19), 2476-2486, doi: 10.1016/j.quascirev.2011.05.017.

Chandler, G., B. L. Markham, and D. L. Helder (2009), Summary of current radiometric calibration coefficients for Landsat MSS, TM, ETM+, and EO-1 ALI sensors, *Remote Sens. Environ.*, *113*(5), 893-903, doi: 10.1016/j.rse.2009.01.007.

Citterio, M., F. Paul, A. P. Ahlstrøm, H. F. Jepsen, and A. Weidick (2009), Remote sensing of glacier change in West Greenland: accounting for the occurrence of surge-type glaciers, *Ann. Glaciol., 50*(53), 70-80.

Citterio, M., and A. P. Ahlstrøm (2013), Brief communication: The aerophotogrammetric map of Greenland ice masses, *The Cryosphere, 7*(2), 445-449, doi: 10.5194/tc-7-445/2013.

Csatho, B., C. J. Van der Veen, and C. M. Tremper (2005), Trimline mapping from multispectral Landsat ETM+ imagery, *Géographie physique et Quaternaire, 59*(1), 49-62, doi:10.7202/013736ar.

Csatho, B., T. Schenk, C. J. Van der Veen, and W. B. Krabill (2008), Intermittent thinning of Jakobshavn Isbræ, West Greenland, since the Little Ice Age, *J. Glaciol., 54*(184), 131-144, doi:10.3189/002214308784409035.

Flint, R. F. (1971), *Glacial and Quaternary Geology*, John Wiley and Sons, New York.

Forman, S. L., L. Marín, C. Van der Veen, C. Tremper, and B. Csatho (2007), Little Ice Age and neoglacial landforms at the Inland Ice margin, Isunguata Sermia, Kangerlussuaq, west Greenland, *Boreas, 36*(4), 341-351, doi: 10.1080/00173130601173301.

Grove, J. M. (2001), The initiation of the "Little Ice Age" in regions around the North Atlantic, *Climatic Change, 48*(1), 53-82, doi:10.1023/A:1005662822136.

Hanna, E., F. J. Navarro, F. Pattyn, C. M. Domingues, X. Fettweis, E. R. Ivins, R. J. Nicholls, C. Ritz, B. Smith, S. Tulaczyk, P. L. Whitehouse, and H. J. Zwally (2013), Ice-sheet mass balance and climate change, *Nature, 498*(7452), 51-59, doi:10.1038/nature12238.

Holland, D. M., R. H. Thomas, B. De Young, M. H. Ribergaard, and B. Lyberth (2008), Acceleration of Jakobshavn Isbræ triggered by warm subsurface ocean waters, *Nat. Geosci., 1*(10), 659-664, doi:10.1038/ngeo316.

Holland, M. M., and C. M. Bitz (2003), Polar amplification of climate change in coupled models, *Climate Dynam., 21*(3-4), 221-232, doi:10.1007/s00382-003-0332-6.

Howat, I. M., and A. Eddy (2011), Multi-decadal retreat of Greenland's marine-terminating glaciers, *J. Glaciol., 57*(203), 389-396.

Howat, I. M., I. Joughin, S. Tulaczyk, and S. Gogineni (2005), Rapid Retreat and acceleration of Helheim Glacier, east Greenland, *Geophys. Res. Lett., 32*(22), L22502, doi:10.1029/2005GL024737.

Howat, I. M., A. Negrete, and B. E. Smith (2014), The Greenland Ice Mapping Project (GIMP) land classification and surface elevation datasets, *The Cryosphere Discuss., 8*, 453-478, doi:10.5194/tcd-8-453-2014.

IPCC (2013), Climate Change 2013: The Physical Science Basis, Contribution of Working Group I to the Fifth Assessment Report of the Intergovernmental Panel on Climate Change [Stocker, T. F., D. Qin, G.-K. Plattner, M. Tignor, S. K. Allen, J. Boschung, A. Nauels, Y. Xia, V. Bex, and P. M. Midgley (eds.)], *Cambridge University Press,* Cambridge, United Kingdom and New York, NY, USA, 1535 pp.

Johannessen, O. M., M. Babiker, and M. W. Miles (2011), Petermann Glacier, North Greenland: massive calving in 2010 and the past half century, *The Cryosphere Discuss., 5*, 169-181, doi:10.5194/tcd-5-169-2011.

Jones, P. D., and A. Moberg (2003), Hemispheric and large-scale surface air temperature variations: An extensive revision and an update to 2001, *J. Clim., 16*(2), 206-223, doi:10.1175/1520-0442(2003)016<0206:HALSSA>2.0.CO;2.

Joughin, I., I. M. Howat, M. Fahnestock, B. Smith, W. Krabill, R. B. Alley, H. Stern, and M. Truffer (2008), Continued evolution of Jakobshavn Isbræ following its rapid speedup, *J. Geophys. Res.*, 113, F04006, doi:10.1029/2008JF001023.

Joughin, I., B. E. Smith, I. M. Howat, T. Scambos, and T. Moon (2010), Greenland flow variability from ice-sheet-wide velocity mapping, *J. Glaciol., 56*(197), 415-430.

Joughin, I., B. E. Smith, D. E. Shean, and D. Floricioiu (2014), Brief communication: Further summer speedup of Jakobshavn Isbræ, *The Cryosphere, 8*, 209-214, doi:10.5194/tc-8-209-2014.

Kamp, U., M. Byrne, and T. Bolch (2011), Glacier Fluctuations between 1975 and 2008 in the Greater Himalaya Range of Zanskar, Southern Ladakh, *J. Mt. Sci., 8*(3), 374-389, doi:10.1007/s11629-011-2007-9.

Kargel, J. S., A. P. Ahlstrøm, R. B. Alley, J. L. Bamber, T. J. Benham, J. E. Box, C. Chen, P. Christoffersen, M. Citterio, J. G. Cogley, H. Jiskoot, G. J. Leonard, P. Morin, T. Scambos, T. Sheldon, and I. Willis (2012), Greenland's shrinking ice cover: "fast times" but not that fast, *The Cryosphere, 6*(3), 533-537, doi: 10.5194/tc-6-533-2012.

Kelley, S. E., J. P. Briner, N. E. Young, G. S. Babonis, and B. Csatho (2012), Maximum late Holocene extent of the western Greenland Ice Sheet during the late 20th century, *Quat. Sci. Rev., 56*, 89-98, doi:10.1016/j.quascirev.2012.09.016.

Kjær, K. H., S. A. Khan, N. J. Korsgaard, J. Wahr, J. L. Bamber, R. Hurkmans, M. van den Broeke, L. H. Timm, K. K. Kjeldsen, A. A. Bjørk, N. K. Larsen, L. T. Jørgensen, A. Færch-Jensen, and E. Willerslev (2012), Aerial photographs reveal late-20th-century dynamic ice loss in northwestern Greenland, *Science, 337*(6094), 569-573, doi:10.1126/science.1220614

Knipling, E. B. (1970), Physical and physiological basis for the reflectance of visible and near-infrared radiation from vegetation, *Remote Sens. Environ., 1*(3), 155-159, doi:10.1016/S0034-4257(70)80021-9.

Kobashi, T., K. Kawamura, J. P. Severinghaus, J. M. Barnola, T. Nakaegawa, B. M. Vinther, S. J. Johnsen, and J. E. Box (2011), High variability of Greenland surface temperature over the past 4000 years estimated from trapped air in an ice core, *Geophys. Res. Lett., 38*, L21501, doi:10.1029/2011GL049444.

Lea, J. M., D. W. F. Mair, F. M. Nick, B. R. Rea, A. Weidick, K. H. Kjær, A. Morlighem, D. Van As, and F. E. Schofield (2014), Terminus-driven retreat of a major southwest Greenland tidewater glacier during the early 19th century: insights from glacier reconstructions and numerical modeling, *J. Glaciol., 60*(220), 333-344, doi:10.3189/2014JoG13J163.

Lemke, P., J. Ren, R. B. Alley, I. Allison, J. Carrasco, G. Flato, Y. Fujii, G. Kaser, P. Mote, R. H. Thomas, and T. Zhang (2007), Observations: Changes in snow, ice and frozen ground, in Climate Change 2007: The Physical Science Basis, Contribution of Working Group I to the Fourth Assessment Report of the Intergovernmental Panel on Climate Change, [Solomon, S., D. Qin, M. Man-

ning, Z. Chen, M. Marquis, K.B. Averyt, M. Tignor and H.L. Miller (Eds.)], *Cambridge University Press*, Cambridge, United Kingdom and New York, NY, USA, 337-383.

Ljungqvist, F. C., P. J. Krusic, G. Brattström, and H. S. Sundqvist (2012), Northern Hemisphere temperature patterns in the last 12 centuries, *Clim. Past, 8*, 227–249, doi:10.5194/cp-8-227-2012.

Mann, M. E., Z. Zhang, S. Rutherford, R. S. Bradley, M. K. Hughes, D. Shindell, C. Ammann, G. Faluvegi, and F. Ni (2009), Global signatures and dynamical origins of the Little Ice Age and Medieval Climate Anomaly, *Science, 326*(5957), 1256-1260, doi:10.1126/science.1177303.

Markham, B. L., J. C. Storey, D. L. Williams, and J. R. Irons (2004), Landsat sensor performance: history and current status, *IEEE Trans. Geosci. Remote Sens., 42*(12), 2691-2694, doi:10.1109/TGRS.2004.840720.

Maurer, J. (2007), Atlas of the Cryosphere, Boulder, Colorado USA, National Snow and Ice Data Center, digital media.

Moon, T., and I. Joughin (2008), Changes in ice front position on Greenland's outlet glaciers from 1992 to 2007, *J. Geophys. Res.*, 113, F02022, doi: 10.1029/2007JF000927.

Moon, T., I. Joughin, B. Smith, and I. Howat (2012), 21st-century evolution of Greenland outlet glacier velocities, *Science, 336*(6081), 576-578, doi: 10.1126/science.1219985.

National Research Council (NRC; 2012), Sea-Level Rise for the Coasts of California, Oregon, and Washington: Past, Present, and Future, *The National Academies Press*, Washington, DC.

Nielsen K., S. A. Khan, G. Spada, J. Wahr, M. Bevis, L. Liu, and T. van Dam (2013), Vertical and horizontal surface displacements near Jakobshavn Isbræ driven by melt-induced and dynamic ice loss, *J. Geophys. Res.-Solid Earth, 118*, 1837-1844, doi:10.1002/jgrb.50145.

Paul, F., N. E. Barrand, S. Baumann, E. Berthier, T. Bolch, K. Casey, H. Frey, S. P. Joshi, V. Konovalov, R. Le Bris, N. Mölg, G. Nosenko, C. Nuth, A. Pope, A. Racoviteanu, P. Rastner, B. Raup, K. Scharrer, S. Steffen, S. Winsvold (2013), On the accuracy of glacier outlines derived from remote-sensing data, *Ann. Glaciol. 54*(63), 171-182, doi:10.3189/2013AoG63A296.

Price, S. F., A. J. Payne, I. M. Howat, and B. E. Smith (2011), Committed sea-level rise for the next century from Greenland ice sheet dynamics during the past decade, *Proc. Natl. Acad. Sci., 108*(22), 8978-8983, doi: 10.1073/pnas.1017313108.

Rae, J. G. L., G. Aðalgeirsdóttir, T. L. Edwards, X. Fettweis, J. M. Gregory, H. T. Hewitt, J. A. Lowe, P. Lucas-Picher, R. H. Mottram, A. J. Payne, J. K. Ridley, S. R. Shannon, W. J. van de Berg, R. S. W. van de Wal, and M. R. van den Broeke (2012), Greenland ice sheet surface mass balance: evaluating simulations and making projections with regional climate models, *The Cryosphere, 6*(3), 2059-2113, doi:10.5194/tc-6-1275-2012.

Sakuma F., A. Ono, S. Tsuchida, N. Ohgi, H. Inada, S. Akagi, and H. Ono (2005), Onboard calibration of the ASTER instrument, *IEEE Trans. Geosci. Remote Sens., 43*(12), 2715-2724, doi:10.1109/TGRS.2005.857887.

Schenk, T., and B. Csatho (2012), A new methodology for detecting ice sheet surface elevation changes from laser altimetry data, *IEEE Trans. Geosci. Remote Sens., 50*(9), 3302-3316, doi:10.1109/TGRS.2011.2182357.

Sohn, H.-G., K. C. Jezek, and C. J. van der Veen (1998), Jakobshavn Glacier, West Greenland: 30 years of Spaceborne observations, *Geophys. Res. Lett. (25)*14, 2699-2702, doi:10.1029/98GL01973.

Sole, A., T. Payne, J. Bamber, P. Nienow, and W. Krabill (2008), Testing hypotheses of the cause of peripheral thinning of the Greenland Ice Sheet: is land-terminating ice thinning at anomalously high rates?, *The Cryosphere, 2*(2), 205-218.

Stewart, H. A. M. (2009), Climate vs. dynamic forcing of Greenland's largest glacier: a study of Jakobshavn Isbræ's response to the Little Ice Age, MS thesis, Department of Geology, University at Buffalo.

Tedstone, A. J., P. W. Nienow, A. J. Sole, D. W. F. Mair, T. R. Cowton, I. D. Bartholomew, and M. A. King (2013), Greenland ice sheet motion insensitive to exceptional meltwater forcing, *Proc. Natl. Acad. Sci., 110*(49), 19719-19724, doi:10.1073/pnas.1315843110.

Ten Brink, N. W., and A. Weidick (1974), Greenland Ice Sheet history since the last glaciation, *Quat. Res. 4*(4), 429-440, doi:10.1016/0033-5894(74)90038-6.

Thomas, R., E. Frederick, W. Krabill, S. Manizade, and C. Martin (2009), Recent changes on Greenland outlet glaciers, *J. Glaciol., 55*(189), 147-162.

University of New Hampshire Institute for the Study of Earth, Oceans, and Space, "Landsat7_pan," planet.sr.unh.edu.

U.S. Geological Survey, Global Visualization Viewer website: glovs.usgs.gov.

Weidick, A. (1968), Observations on some Holocene glacier fluctuations in West Greenland, *Meddelelser om Grønland, 165*(6).

Weidick, A. (1995), Satellite image atlas of glaciers of the world: Greenland, U.S. Geological Survey Professional Paper 1386-C.

Weidick, A., M. Kelly, and O. Bennike (2004), Late Quaternary development of the southern sector of the Greenland Ice Sheet, with particular reference to the Qassimiut lobe, *Boreas, 33*(4), 284-299, doi:10.1080/03009480410001947.

Young, N. E., J. P. Briner, H. A. M. Stewart, Y. Axford, B. Csatho, D. H. Rood, R. C. Finkel (2011), The response of Jakobshavn Isbræ Greenland, to Holocene climate change, *Geology, 39*(2), 131-134, doi:10.1130/G31399.1.

Zwally, H. J., W. Abdalati, T. Herring, K. Larson, J. Saba, and K. Steffen (2002), Surface melt-induced acceleration of Greenland ice-sheet flow, *Science, 297*(5579), 218-222, doi:10.1126/science.1072708.

Zwally, H. J., J. Li, A. C. Brenner, M. Beckley, H. G. Cornejo, J. DiMarzio, M. B. Giovinetto, T. A. Neumann, J. Robbins, J. L. Saba, D. H. Yi, and W. L. Wang (2011), Greenland ice sheet mass balance: distribution of increased mass loss with climate warming; 2003-07 versus 1992-2002, *J. Glaciol., 57*(201), 88–102.